High-precision continuum limit study of the HVP short-distance window

Sebastian Spiegel[*] and Christoph Lehner[†]
Department of Physics, University of Regensburg, 93040 Regensburg, Germany

(Received 31 October 2024; accepted 22 May 2025; published 24 June 2025)

The separation of the hadronic vacuum polarization contribution to the muon anomalous magnetic moment into Euclidean windows allows for a tailored approach to address the different dominant challenges at short, intermediate, and long distances. We present a novel approach to compute the short-distance window without the need for using perturbative QCD. We combine a quenched continuum extrapolation using 18 lattice spacings ($1.6\ \mathrm{GeV} \lesssim a^{-1} \lesssim 6.1\ \mathrm{GeV}$) with a separate continuum extrapolation of the sea quark effects. This method allows for the computationally expensive sea quark effects to be estimated using only a smaller number of ensembles at coarser lattice spacings, while largely confining the logarithmic dependency of the continuum extrapolation to the quenched component.

DOI: 10.1103/mj3d-yq87

I. INTRODUCTION

The magnetic moment of the muon is defined by

$$\boldsymbol{\mu} = -g_\mu \frac{e}{2m_\mu} \boldsymbol{S}, \tag{1}$$

where e is the electric charge, m_μ is the muon mass, $\boldsymbol{S}$ is the particle's spin, and g_μ denotes its Landé factor. The deviation with Dirac's result of $g_\mu = 2$ is defined as the anomalous magnetic moment of the muon,

$$a_\mu = \frac{g_\mu - 2}{2}, \tag{2}$$

which captures the radiative corrections of all known and unknown particles. This quantity is one of the most precisely determined values in physics and plays an important role in high-precision tests of our understanding of physics at the fundamental level. The latest experimental results provided by FNAL Muon g-2 collaboration, which combine their first two publications [1,2] with the final result of the BNL E821 experiment [3], arrive at a precision of 0.19 parts per million (ppm) for the world average.

In contrast, the recommended Standard Model result of the Muon g-2 Theory Initiative from 2020 [4] has an uncertainty of 0.37 ppm. To match the precision of the experimental measurement, the theoretical uncertainty must be reduced by roughly half. This, combined with the anticipated progress from the planned J-PARC experiment [5], underscores the need for novel methods to improve the theoretical uncertainty. The leading-order hadronic vacuum polarization (HVP) predominantly contributes to the theoretical prediction's uncertainty, making its refinement particularly urgent.

Using the Euclidean window approach introduced by RBC/UKQCD collaborations in [6], this quantity can be divided into three subcontributions: short-distance, window, and long-distance contributions. This allows to separate the challenging short- and long-distance quantities from the window quantity, which has tractable statistical and systematic errors. While the discretization effects are most significant for the short-distance contribution, the statistical noise and finite-volume effects are particularly severe in the long-distance contribution. This work aims to scrutinize the continuum limit of the short-distance window from first principles using purely lattice QCD methods, without perturbative input. The approach combines a precise quenched continuum limit, derived from 18 lattice spacings, with a separate continuum extrapolation of the dynamical sea quark corrections, utilizing only a few computationally expensive ensembles.

This paper is organized as follows: in Sec. II, we introduce the methodology of the time-momentum representation for the leading-order HVP, which facilitates the definition of Euclidean windows. The computational details are provided in Sec. III. Subsequently, we present the blinded quenched and sea quark continuum limit results, along with our blinded short-distance HVP results, before unblinding the latter.

[*]Contact author: sebastian.spiegel@ur.de
[†]Contact author: christoph.lehner@ur.de

II. METHODOLOGY

In the following sections, we describe the time-momentum representation (Sec. II A) and define the Euclidean windows (Sec. II B), which provide a basis for computing the short-distance contribution to the leading-order (LO) HVP, $a_\mu^{\mathrm{HVP\,LO}}$. For brevity, we will omit the superscript HVP LO from this point onward.

A. Time-momentum representation

We consider the correlator

$$C(t) = \frac{1}{3}\sum_{\vec{x}}\sum_{j=0,1,2}\langle J_j(\vec{x},t)J_j(0)\rangle, \tag{3}$$

where $J_\mu(x)$ denotes the vector current, defined as

$$J_\mu(x) = i\sum_f Q_f \bar{\psi}_f(x)\gamma_\mu\psi_f(x). \tag{4}$$

In this expression, Q_f denotes the fractional electric charge, and the sum runs over the quark flavors f. The leading-order HVP contribution to a_μ is then computed as

$$a_\mu = \sum_{t=0}^{\infty} w_t C(t). \tag{5}$$

The weights w_t incorporate the photon and muon effects within the HVP diagrams and can be computed via the integral [7]

$$w_t = 8\alpha^2\int_0^\infty \mathrm{d}Q^2\left(\frac{\cos(Qt)-1}{Q^2}+\frac{1}{2}t^2\right)f(Q), \tag{6}$$

where Q^2 denotes the Euclidean photon four-momentum squared, $Q \equiv |Q|$ is the magnitude of the Euclidean four-momentum, and α is the fine structure constant. The function $f(Q)$ is given by

$$f(Q) = \frac{m_\mu^2 Q^2 Z^3(Q)(1-Q^2Z(Q))}{1+m_\mu^2Q^2Z^2(Q)}$$
$$\text{with}\quad Z(Q) = \frac{\sqrt{Q^4+4Q^2m_\mu^2}-Q^2}{2m_\mu^2Q^2}. \tag{7}$$

Here, m_μ abbreviates the muon mass. Additionally, we consider an alternative weight definition

$$\hat{w}_t = 8\alpha^2\int_0^\infty \mathrm{d}Q^2\left(\frac{\cos(Qt)-1}{(2\sin(Q/2))^2}+\frac{1}{2}t^2\right)f(Q), \tag{8}$$

which uses a lattice discretization of the photon momentum and yields the same value of a_μ in the continuum limit. Using both weight definitions allows us to investigate the continuum limit and test the robustness of our analysis approach.

In this study, we compute the up and down quark-connected contribution to the correlator $C(t)$ in the isospin-symmetric limit. For brevity, we omit an explicit label in the notation.

B. Euclidean windows

In line with the method outlined in [6], we utilize Euclidean windows to separate the contributions from time slices t in Eq. (5) into short-distance (SD), window (W), and long-distance (LD) components. We apply smearing kernels with a width Δ to ensure well-defined quantities at nonzero lattice spacing. This approach leads to the partitioning

$$a_\mu = a_\mu^{\mathrm{SD}} + a_\mu^{\mathrm{W}} + a_\mu^{\mathrm{LD}} \tag{9}$$

with the individually well-defined contributions

$$a_\mu^{\mathrm{SD}}(t_0,\Delta) = \sum_{t=0}^{\infty} C(t)w_t[1-\Theta(t,t_0,\Delta)], \tag{10}$$

$$a_\mu^{\mathrm{W}}(t_0,t_1,\Delta) = \sum_{t=0}^{\infty} C(t)w_t[\Theta(t,t_0,\Delta)-\Theta(t,t_1,\Delta)], \tag{11}$$

$$a_\mu^{\mathrm{LD}}(t_1,\Delta) = \sum_{t=0}^{\infty} C(t)w_t\Theta(t,t_1,\Delta), \tag{12}$$

$$\Theta(t,t',\Delta) = [1+\tanh[(t-t')/\Delta]]/2. \tag{13}$$

This work focuses on determining the short-distance segment $a_\mu^{\mathrm{SD}}(t_0,\Delta)$, relying exclusively on lattice methods. Among the contributions, discretization effects are expected to be most severe for this segment. For our analysis, we use the values $t_0 = 0.4$ fm and $\Delta = 0.15$ fm [6].

III. COMPUTATIONAL DETAILS

In the following, the computational details of this work are discussed. This includes ensemble generation, an overview of the analyzed measurements, as well as crucial aspects of the analysis.

A. Data description

The quenched ensembles for this study were generated using the hybrid Monte Carlo (HMC) algorithm [8] and the Iwasaki gauge action. Each molecular dynamics (MD) trajectory was evolved for a time of $\tau = 1.0$ using 12 steps of a fourth-order Omelyan integrator [9]. A total of 21 quenched ensembles with lattice spacings ranging from $a^{-1} \approx 1.57$ to 6.10 GeV were generated, with an overview provided in Table I. Among these ensembles, nine have periodic boundary conditions (periodic BC) and a lattice

TABLE I. List of quenched ensembles with simulation parameters. The ensembles were generated using the Iwasaki gauge action, and their lattice spacing was determined employing the gradient flow scale t_0 with physical input from [10–12]. The columns represent the inverse coupling (β), the inverse lattice spacing (a^{-1}/GeV), the gradient flow scales ($\sqrt{t_0}/a$ and w_0/a), the lattice volume ($L^3 \times T/a^4$), the BCs, and the sample sizes for gluonic (N_{gluonic}) and fermionic ($N_{\mathrm{fermionic}}$) measurements.

β	a^{-1}/GeV	$\sqrt{t_0}/a$	w_0/a	$L^3 \times T/a^4$	BC	N_{gluonic}	$N_{\mathrm{fermionic}}$
2.40	1.5677(95)	1.30154(53)	1.28618(72)	$24^3 \times 48$	Periodic	200	100
2.45	1.691(11)	1.40422(80)	1.3931(12)	$24^3 \times 48$	Periodic	200	100
2.50	1.824(12)	1.5139(10)	1.5068(15)	$24^3 \times 48$	Periodic	200	100
2.55	1.966(13)	1.6324(11)	1.6313(16)	$24^3 \times 48$	Periodic	200	100
2.60	2.109(13)	1.7507(16)	1.7523(24)	$24^3 \times 48$	Periodic	200	100
2.65	2.265(14)	1.8807(20)	1.8881(30)	$24^3 \times 48$	Periodic	200	200
2.70	2.425(16)	2.0136(26)	2.0239(36)	$24^3 \times 48$	Periodic	200	100
2.75	2.601(17)	2.1595(34)	2.1764(50)	$24^3 \times 48$	Periodic	200	100
2.80	2.781(18)	2.3091(36)	2.3303(53)	$24^3 \times 48$	Periodic	420	220
2.80	2.780(18)	2.3083(40)	2.3254(59)	$24^3 \times 96$	Open	200	230
2.85	2.969(20)	2.4652(58)	2.4835(82)	$24^3 \times 96$	Open	200	200
2.90	3.184(22)	2.6434(71)	2.6739(91)	$24^3 \times 96$	Open	200	200
2.95	3.394(24)	2.8179(90)	2.849(13)	$24^3 \times 96$	Open	200	200
3.00	3.650(26)	3.0303(97)	3.077(15)	$24^3 \times 96$	Open	200	200
3.05	3.901(30)	3.238(15)	3.289(22)	$24^3 \times 96$	Open	200	200
3.10	4.142(32)	3.439(16)	3.492(23)	$24^3 \times 96$	Open	200	400
3.15	4.462(43)[a]	3.704(28)[a]	3.780(42)[a]	$24^3 \times 96$	Open	200	200
3.00	3.635(24)	3.0174(74)	3.055(11)	$32^3 \times 96$	Open	200	200
3.15	4.433(31)	3.680(13)	3.74(18)	$32^3 \times 96$	Open	200	300
3.20	4.737(39)[a]	3.932(21)[a]	4.004(30)[a]	$32^3 \times 96$	Open	200	400
3.40	6.099(43)[a]	5.063(17)[a]	5.139(25)[a]	$48^3 \times 192$	Open	200	200

[a]Indicates that in these cases, the binning study did not conclusively converge for the scale setting parameters themselves, cf. Table III. We address this issue by using the delayed binning strategy described in the following.

volume of $24^3 \times 48$. The inverse couplings for these ensembles range from $\beta = 2.40$ to $\beta = 2.80$ in steps of 0.05. Additionally, eight ensembles with open boundary conditions (open BC) and a lattice volume of $24^3 \times 96$ were generated, with β values ranging from 2.80 to 3.15, also in steps of 0.05. To further refine our analysis, three additional open BC ensembles with inverse couplings $\beta = 3.0$, 3.15, and 3.2 were generated using a larger lattice volume of $32^3 \times 96$. Finally, an ensemble with a lattice volume of $48^3 \times 192$ at $\beta = 3.4$ was generated, also with open BC.

To decrease autocorrelations, only every 100th generated MD trajectory was considered for subsequent analyses of each ensemble, except for $\beta = 3.4$ where only every 250th was retained. The binning study presented in Table III demonstrates that this choice ensures sufficiently small autocorrelations for the analyzed gradient flow observables. Thermalization of the Markov chains was decided based on gradient flow scale measurements (cf. Sec. III C) on each configuration. For open BC ensembles, all measurements were performed within their respective bulk, which we define by the time slices $[\frac{T}{2a} - \frac{L}{a}, \frac{T}{2a} + \frac{L}{a}]$, unless indicated otherwise.

The analysis presented consists of two main types of measurements: purely gluonic measurements based on the energy density and vector correlator measurements. For the gluonic measurements, every second available configuration was used to further reduce correlations. The fermionic measurements were performed on consecutive configurations. The last two columns of Table I show the sample sizes for both gluonic and fermionic measurements. For the fermionic measurements, we employed Möbius [13] domain-wall [14,15] fermions with parameters $b = 1.5$ and $c = 0.5$. The length of the fifth dimension, which controls residual chiral-symmetry-breaking effects, was set to $L_s = 12$ for all quenched ensembles. We verified that the residual chiral-symmetry-breaking effects are small even for the finest lattice ensemble by evaluating the correlators at $\beta = 3.4$ also with $L_s = 24$. All observed variations were sub-per-mille.

In our analysis, we use four dynamical ensembles that were generated using the Iwasaki gauge action and Möbius domain-wall fermion sea quarks. These ensembles employ $N_f = 2 + 1$ sea quark flavors, with lattice spacings ranging from $a^{-1} \approx 1.73$ to 3.53 GeV. A detailed description of

TABLE II. List of dynamical ensembles with simulation parameters. The ensembles were generated using the Iwasaki gauge action and Möbius domain-wall fermion sea quarks with $2+1$ flavors. The columns represent the ensemble identifier (ID), the inverse lattice spacing (a^{-1}/GeV), the gradient flow scales ($\sqrt{t_0}/a$ and w_0/a), the lattice dimensions ($L^3 \times T \times L_s/a^4$), the BCs, the number of considered gauge field configurations (N_{cfg}), and the pion and kaon masses (M_π and M_K) in MeV. For these dynamical ensembles, the number of gluonic and fermionic measurements is identical and is, therefore, summarized in a single variable N_{cfg}.

ID	a^{-1}/GeV	$\sqrt{t_0}/a$	w_0/a	$L^3 \times T \times L_s/a^4$	BC	N_{cfg}	M_π/MeV	M_K/MeV
4	1.7312(28)	1.2880(09)	1.4758(20)	$24^3 \times 48 \times 24$	Periodic	104	274.8(2.5)	530.1(3.1)
9	2.3549(49)	1.7335(09)	2.0206(20)	$32^3 \times 64 \times 12$	Periodic	141	278.79(62)	530.98(75)
F	2.6920(67)	1.9907(04)	2.3583(08)	$48^3 \times 96 \times 12$	Periodic	20	283.2(1.0)	519.3(1.4)
E	3.53(01)	2.5678(28)	3.0254(76)	$48^3 \times 192 \times 12$	Open	40	289.5(2.1)	540.0(2.5)

ensemble 4 can be found in [16], while the other ensembles were produced with similar codes. Table II provides an overview of the dynamical ensembles, along with their properties.

B. Statistical and systematic errors

To obtain statistical error estimates on the measured observables, we rely on a modified version of the jackknife method. For n different observables O_i with $i = 1, \ldots n$, we consider the sample means

$$\bar{O}_i = \frac{1}{|S|}\sum_{\tau \in S} O_i^\tau, \tag{14}$$

where S denotes a selection of thermalized Markov times τ. The covariance of two such observables O_i and O_j may be estimated using

$$\overline{\mathrm{Cov}}(O_i, O_j) = \frac{1}{|S|-1}\sum_{\tau \in S}(O_i^\tau - \bar{O}_i)(O_j^\tau - \bar{O}_j). \tag{15}$$

Consider now a function

$$\bar{f}_\alpha = f_\alpha(\bar{O}_1, \ldots, \bar{O}_n), \tag{16}$$

for which we also wish to estimate the corresponding covariance. The standard jackknife estimation procedure consists of computing the single-elimination jackknife average defined according to

$$\bar{O}_i^{(\tau)} = \frac{1}{|S|-1}(|S|\bar{O}_i - O_i^\tau) = \bar{O}_i + \frac{1}{|S|-1}(\bar{O}_i - O_i^\tau), \tag{17}$$

and correspondingly

$$\bar{f}_\alpha^{(\tau)} = f_\alpha(\bar{O}_1^{(\tau)}, \ldots, \bar{O}_n^{(\tau)}). \tag{18}$$

The jackknife estimate for the covariance between $\bar{f}_\alpha$ and $\bar{f}_\beta$ is subsequently given by

$$\overline{\mathrm{Cov}}(\bar{f}_\alpha, \bar{f}_\beta) = \frac{|S|-1}{|S|}\sum_{\tau \in S}(\bar{f}_\alpha^{(\tau)} - \bar{f}_\alpha)(\bar{f}_\beta^{(\tau)} - \bar{f}_\beta). \tag{19}$$

This method assumes that the Markov time selection S is chosen in such a way that all data are uncorrelated. In practice, however, this is often not the case. One way to remedy this is by employing a binning procedure and studying the covariances as a function of the bin size m to identify a plateau for large m. Incorporating the binning of the data with the jackknife average definition in a single step allows to define the m-elimination jackknife average

$$\begin{aligned}\bar{O}_i^{(\tau_1,\ldots,\tau_m)} &= \frac{1}{|S|-m}\left(|S|\bar{O}_i - \sum_{k=1}^{m} O_i^{\tau_k}\right) \\ &= \bar{O}_i + \frac{1}{|S|-m}\left(m\bar{O}_i - \sum_{k=1}^{m} O_i^{\tau_k}\right).\end{aligned} \tag{20}$$

This can be used to compute $\bar{f}_\alpha^{(\tau_1,\ldots,\tau_m)}$ and subsequently the jackknife estimate for the covariance. However, this procedure requires prior knowledge of the appropriate bin size to ensure data independence, as correlations between subsequent measurements vary by observable. To address this, we reconstruct the m-elimination jackknife sample using the formula

$$\begin{aligned}\bar{f}_\alpha^{(\tau_1,\ldots,\tau_m)} &= \bar{f}_\alpha + \frac{|S|-1}{|S|-m}\left(\sum_{k=1}^{m}\bar{f}_\alpha^{(\tau_k)} - m\bar{f}_\alpha\right) \\ &\quad + \mathcal{O}\left(\frac{1}{(|S|-1)(|S|-m)}\right).\end{aligned} \tag{21}$$

This approach allows us to delay the binning in the jackknife method and compute $\bar{f}_\alpha^{(\tau_1,\ldots,\tau_m)}$ directly from the unbinned $\bar{f}_\alpha^{(\tau)}$. Consequently, only unbinned jackknife samples need to be stored, which enables us to study autocorrelations using the reconstructed binned jackknife sample.

Next, we briefly discuss the treatment of systematic errors in our analysis. These errors arise from external inputs, modeling assumptions, or computational methods.

TABLE III. Binning study for the gradient flow scales $\sqrt{t_0}/a$ and w_0/a for each quenched ensemble. The table columns show the inverse coupling (β), the rescaled standard deviations of the gradient flow scales [$\sigma_b(\sqrt{t_0}/a)$ and $\sigma_b(w_0/a)$] for bin sizes $b = 1, 2, 4, 8$, the lattice volume ($L^3 \times T/a^4$), and the BCs. The standard deviations were scaled by a factor of 10^4 and the values chosen for the analysis, such as those given in Table I, are indicated with a star. The maximum bin size for the study was chosen such that the binned samples contained at least 25 entries, ensuring a sufficiently small error in the estimated uncertainties.

	$\sigma_b(\sqrt{t_0}/a) \times 10^4$				$\sigma_b(w_0/a) \times 10^4$					
β	$b=1$	$b=2$	$b=4$	$b=8$	$b=1$	$b=2$	$b=4$	$b=8$	$L^3 \times T/a^4$	BC
2.40	4.92★	5.21	5.55	5.41	6.75★	7.14	7.62	7.51	$24^3 \times 48$	Periodic
2.45	7.10	7.98★	8.97	9.30	9.93	11.18★	12.56	13.67	$24^3 \times 48$	Periodic
2.50	8.32	9.97★	10.21	10.46	11.87	14.14★	14.44	15.47	$24^3 \times 48$	Periodic
2.55	10.12	10.92★	10.62	11.81	14.45	15.64★	15.32	16.98	$24^3 \times 48$	Periodic
2.60	12.38	13.99	15.60★	15.40	18.42	21.07	23.55★	22.74	$24^3 \times 48$	Periodic
2.65	16.50	19.61	19.69★	22.60	22.80	26.78	29.22★	32.87	$24^3 \times 48$	Periodic
2.70	19.40	22.03	25.48★	25.27	26.83	30.74	35.79★	37.23	$24^3 \times 48$	Periodic
2.75	24.63	29.75	33.58★	34.76	33.76	42.39	49.48★	54.19	$24^3 \times 48$	Periodic
2.80	22.19	27.57	33.15	35.21★	31.45	39.37	48.01	52.39★	$24^3 \times 48$	Periodic
2.80	30.74	35.20	39.83	39.24★	43.75	51.24	59.06	58.42★	$24^3 \times 96$	Open
2.85	41.94	51.30	60.40	57.63★	57.85	72.03	84.25	81.88★	$24^3 \times 96$	Open
2.90	44.61	52.96	61.25	70.65★	60.41	72.33	82.31	90.19★	$24^3 \times 96$	Open
2.95	56.26	69.87	81.01	89.35★	78.37	97.61	112.45	127.77★	$24^3 \times 96$	Open
3.00	69.22	84.41	94.77	96.74★	100.13	125.37	140.99	142.14★	$24^3 \times 96$	Open
3.05	87.31	109.82	130.14	142.98★	128.27	163.95	194.79	216.61★	$24^3 \times 96$	Open
3.10	99.96	124.01	150.85	159.65★	137.75	171.54	212.56	228.42★	$24^3 \times 96$	Open
3.15	140.07	177.77	220.03	275.18★	206.32	263.96	330.91	415.67★	$24^3 \times 96$	Open
3.00	46.18	55.94	62.92	73.93★	64.53	79.90	93.10	107.71★	$32^3 \times 96$	Open
3.15	84.86	104.89	121.76	127.76★	112.30	141.04	159.28	174.79★	$32^3 \times 96$	Open
3.20	96.97	127.19	159.88	209.15★	139.12	182.97	235.70	298.83★	$32^3 \times 96$	Open
3.40	85.56	105.15	135.34	165.79★	118.44	152.32	199.00	244.94★	$48^3 \times 192$	Open

Given that their values are much smaller compared to the sample means, we assume that derived quantities can be linearized for sufficiently small deviations from the mean. To propagate systematic errors to a function dependent on these means, we use the following approach for each systematic error: compute the function at the mean plus the systematic error, then compute the quadratic difference between this result and the function evaluated at the mean. This quadratic difference is treated as the variance, assuming that systematic errors are symmetrically distributed around the mean. A given estimate of a derived quantity may involve multiple systematic errors, either propagated from quantities it depends on or arising at the current computational step. These systematic errors are treated as independent and are, therefore, combined in quadrature to yield the total systematic error.

When quoting results, we present the mean value followed by two parentheses: the first contains the statistical error and the second contains the total systematic error. The total variance, obtained by summing the statistical and systematic variances in quadrature, is used for error bars in plots unless explicitly stated otherwise. Numerical results, however, are quoted with the errors presented separately.

C. Scale setting

The scale in this analysis is set using the gradient flow scales t_0 and w_0. The scale t_0 is defined [12] by the condition

$$t^2\langle E(t)\rangle|_{t=t_0} = 0.3, \tag{22}$$

where $E(t)$ denotes the Wilson flow smeared energy density at flow time t. Similarly, the scale w_0 is defined by the condition [17]

$$t\frac{d}{dt}(t^2\langle E(t)\rangle)|_{t=w_0^2} = 0.3. \tag{23}$$

We calculate the energy density $E(t)$ on the lattice using the cloverleaf definition, as follows:

$$E(t) = -\frac{1}{2|\Lambda|}\sum_{x\in\Lambda}\sum_{\mu<\nu}\mathrm{tr}\left[\tilde{F}^{\mathrm{clover}}_{\mu\nu}(x)\tilde{F}^{\mathrm{clover}}_{\mu\nu}(x)\right], \tag{24}$$

where Λ denotes the set of sites of the lattice under consideration, $|\Lambda|$ the number of grid sites, and $\tilde{F}^{\mathrm{clover}}_{\mu\nu}(x) = A_{\mu\nu}(x) - A^{\dagger}_{\mu\nu}(x)$. Here, $A_{\mu\nu}(x)$ is the average

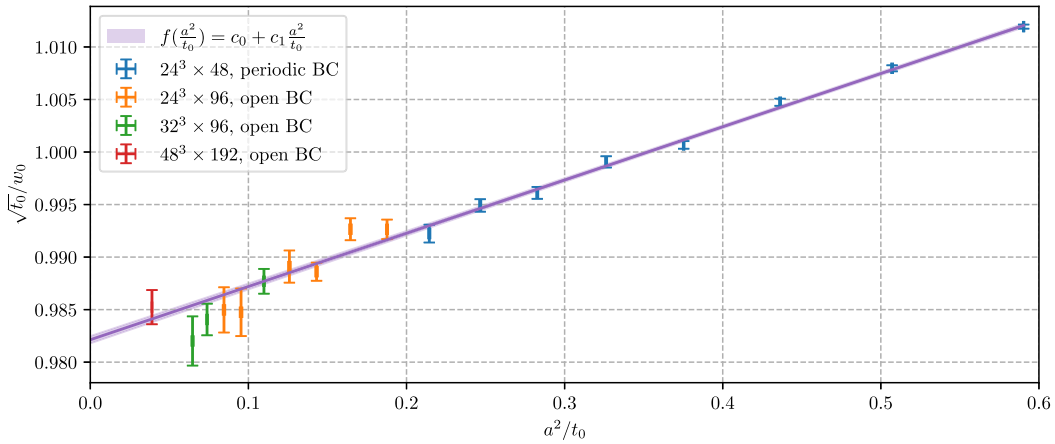

FIG. 1. Continuum extrapolation of $\sqrt{t_0}/w_0$ with the linear fit model $f(a^2/t_0) = c_0 + c_1 a^2/t_0$.

of the oriented plaquettes in the $\mu - \nu$ plane centered at lattice site x,

$$A_{\mu\nu}(x) = \frac{1}{4}\left(U_{\mu\nu}(x) + U_{\nu-\mu}(x) + U_{-\nu\mu}(x) + U_{-\mu-\nu}(x)\right). \tag{25}$$

The plaquette $U_{\mu\nu}(x)$ is constructed as

$$U_{\mu\nu}(x) = U_\mu(x) U_\nu(x + a\hat{\mu}) U_{-\mu}(x + a\hat{\mu} + a\hat{\nu}) U_{-\nu}(x + a\hat{\nu}), \tag{26}$$

where $U_\mu(x)$ are the gauge link variables on the lattice, and the inverse link variable is defined as $U_{-\mu}(x) = U_\mu^\dagger(x - a\hat{\mu})$. For ensembles with open BC, the lattice site averaging is restricted to the bulk.

We noted above that the thermalization of Markov chains was determined based on the gradient flow scales. For this purpose, a modified version of the scales was used, where the statistical average over the energy density was replaced by the energy density of a single configuration at each Markov time. These quantities exhibit particularly slow Markov modes compared to other observables considered in this work.

The third and fourth columns of Table I show the determined estimates of $\sqrt{t_0}/a$ and w_0/a for the quenched ensembles. For ensembles marked with an ([a]), the binning study for the scale quantities did not convincingly converge, cf. Table III. Specifically, these ensembles include the ensembles at $\beta = 3.15$ with a lattice volume of $24^3 \times 96$, $\beta = 3.2$ with a lattice volume of $32^3 \times 96$, and $\beta = 3.4$ with a lattice volume of $48^3 \times 192$. This observation is based on a binning analysis, where the maximum bin size for each ensemble was chosen such that the binned samples had a size of at least 25 to ensure a sufficiently small error on the error. All subsequent binning studies mentioned in this work were performed in the same manner. However, this observation does not impact subsequent parts of this work, as the delayed binning in the jackknife can be applied separately for derived quantities depending on the flow scale. For such derived quantities, the delayed binning study did not indicate residual autocorrelations, such that the observation only limits the precision with which we can quote the scale quantities. In Fig. 1, we illustrate the continuum extrapolation of the dimensionless ratio $\sqrt{t_0}/w_0$ as a function of a^2/t_0 using a linear model

$$f\left(\frac{a^2}{t_0}\right) = c_0 + c_1 \frac{a^2}{t_0}. \tag{27}$$

As a^2/t_0 approaches zero, the extrapolated value of $\sqrt{t_0}/w_0$ converges to a finite continuum limit. For the inverse coupling $\beta = 2.8$, the open BC measurements were considered, while for $\beta = 3.0$ and $\beta = 3.15$, we used the ensembles with larger lattice volumes. The data show that the lattice effects appear to be of order a^2 over the full range of considered quenched ensembles. To determine the lattice spacing a, we rely on the gradient flow scale t_0. We use the following external input from [10–12] to set the physical value of $\sqrt{t_0}$:

$$\sqrt{t_0} = 0.1638(10)\ \text{fm}. \tag{28}$$

While this choice defines how we translate dimensionful quantities, such as the muon mass, to dimensionless units in the quenched world, our final results are corrected to include dynamical sea quarks and are independent of this choice. Note that one may use the central value of $\sqrt{t_0}$ without uncertainty as the definition of physical distance for our intermediate quenched world.

In Fig. 2, we present an interpolation of a^{-1}/GeV derived from $\sqrt{t_0}$ versus β. The β values range from 2.4 to 3.4. For $\beta = 2.8$, we used the open BC data, and for $\beta = 3.0$ and $\beta = 3.15$, we used the large-volume

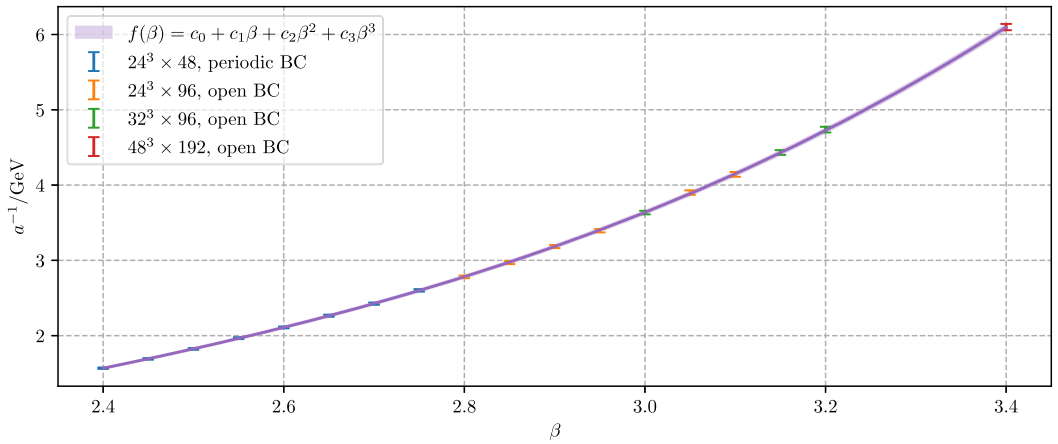

FIG. 2. Interpolation of a^{-1}/GeV derived from $\sqrt{t_0}$ versus β using the cubic fit model $f(\beta) = c_0 + c_1\beta + c_2\beta^2 + c_3\beta^3$.

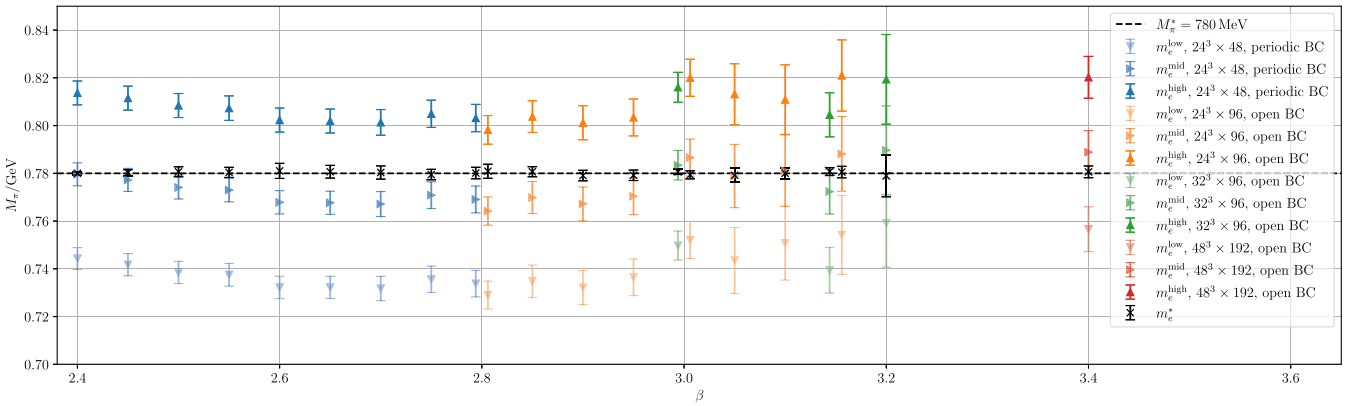

FIG. 3. Pion masses for three different bare quark masses, m_e^{low}, m_e^{mid}, and m_e^{high}, calculated for each quenched ensemble e. We note that for ensembles with the same inverse coupling β, the data points were shifted slightly to enhance visibility. The quark masses were selected such that a single physical pion mass of $M_\pi^* = 780$ MeV could be chosen to lie within the ranges defined by these three quark masses across all 21 ensembles. The plot demonstrates the consistency of the physical pion masses obtained from the quadratically interpolated pion correlators at quark masses m_e^* with M_π^*.

ensembles. The interpolation is performed using a cubic fit model of the form

$$f(\beta) = c_0 + c_1\beta + c_2\beta^2 + c_3\beta^3, \tag{29}$$

with fitted parameters $c_0 = -13.143(12)$, $c_1 = 15.8718(62)$, $c_2 = -6.5925(22)$, and $c_3 = 1.0555(18)$. The p-value of the fit is approximately 0.38.

D. Mass interpolation

Although we expect short-distance correlators to be largely insensitive to the quark mass [16], we aimed to compute the short-distance hadronic vacuum polarization at the same physical mass point across ensembles with different lattice spacings to minimize any potential mass effects. To achieve this, we calculated pion correlators for three different bare quark masses, m_e^{low}, m_e^{mid}, and m_e^{high}, for each quenched ensemble e and determined the corresponding pion masses in physical units, see Fig. 3. The quark masses were selected such that a single physical pion mass M_π^* could be chosen to lie within the ranges defined by the three quark masses for all of the 21 ensembles. This specified physical pion mass was then used to identify the quark mass m_e^* for each quenched ensemble, corresponding to the physical pion mass for that ensemble, via quadratic interpolation. For the given quenched ensembles, we defined the mass point by the physical pion mass of

$$M_\pi^* \equiv 780 \text{ MeV}. \tag{30}$$

We explicitly note that selecting the pion mass involves a careful balance between finite volume effects and mass effects for a_μ^{SD}. Specifically, the chosen value for M_π^* ensures that $M_\pi L \gtrsim 4$ for all considered ensembles. Based on previous studies [16], mass effects are expected to

be small. The resulting quark masses m_e^* allowed us to quadratically interpolate the pion and vector correlation functions for each ensemble to the same mass point. To account for systematic errors associated with the quadratic interpolation, we performed an additional linear interpolation to M_π^* using the data from the two nearest pion masses for each ensemble. The systematic error on the correlators from this step was determined as the square root of the quadratic difference between the results of the linear and quadratic interpolations. This error is included as part of the total systematic error, which is combined in quadrature, as described in Sec. III B. We emphasize that there is flexibility in choosing the quantity used to define the same physical mass point for all ensembles. Instead of the physical pion mass M_π^*, we could also have used dimensionless combinations, such as $\sqrt{t_0}M_\pi^*$.

As a cross-check to test the sensibility of interpolating correlators, as described above, we determined the physical mass of the interpolated pion correlators and verified whether it matched $M_\pi^* = 780$ MeV. As shown in Fig. 3, we were able to retrieve the original mass for all quenched ensembles within the margin of error. We note that the relatively smaller error bars on the pion masses obtained from the interpolated correlation functions arise due to anticorrelations in the bare quark mass m_e^*. These anticorrelations emerge because the jackknife samples of the pion masses are all interpolated to the same fixed physical mass point M_π^*, reducing statistical fluctuations in the final result.

E. Blinding procedure

Before the final datasets were generated, a blinding procedure was put in place. Each author performed a separate analysis with a common blinding factor applied to the correlators. The blinding factor was produced by a noninvertible hash function that was known to one of the authors. The blinding factors themselves were not known to the authors. After cross-checks were performed between the two analyses in a blinded manner, the result was fully unblinded by evaluating the hash function in a Zoom meeting on July 22, 2024.

F. Local- and conserved-current correlators

In our analysis, we consider the local lattice vector correlator J_μ [Eq. (4)], which we will refer to as J_μ^l hereafter, as well as the conserved lattice vector current J_μ^c, as defined in [18]. We study the correlators

$$C^{ab}(t) = \frac{1}{3}\sum_{\vec{x}}\sum_{j=0,1,2}\langle J_j^b(\vec{x},t)J_j^a(0)\rangle, \tag{31}$$

considering their local-local (C^{ll}) and local-conserved (C^{lc}) versions. For both the quenched and dynamical ensembles, we consider the up and down quark-connected contributions to the correlators in the isospin-symmetric limit. For the dynamical correlators, an all-mode-averaging procedure [19–22] is applied. In case of C^{ll}, we use a numerically cheaper but less precise estimator, $C^{\mathrm{ll}}_{\mathrm{sloppy}}$. We compute the difference $C^{\mathrm{ll}} - C^{\mathrm{ll}}_{\mathrm{sloppy}}$ using a single source position for each sample element and then add this difference to our full statistics estimator of $C^{\mathrm{ll}}_{\mathrm{sloppy}}$, which uses multiple sources, to obtain an estimate for C^{ll}. Similarly, we take advantage of the high correlations between the local-local and local-conserved correlators for a specific source position. To estimate C^{lc}, we first evaluate a sloppy estimator by calculating $C^{\mathrm{lc}}_{\mathrm{sloppy}} - C^{\mathrm{ll}}_{\mathrm{sloppy}}$ for a few correlated source positions and adding the full statistics of the computationally cheaper estimator of $C^{\mathrm{ll}}_{\mathrm{sloppy}}$. Subsequently, the difference $C^{\mathrm{lc}} - C^{\mathrm{lc}}_{\mathrm{sloppy}}$ is computed using a single source position for each sample element and added to the sloppy estimate. (The second analysis group used the ratio $C^{\mathrm{lc}}/C^{\mathrm{ll}}$ with smaller statistics combined with the full statistics estimator of C^{ll} to construct the C^{lc} estimator.)

To determine the renormalization factor Z_V, we extract the constant from the ratio C^{lc}/C^{ll}, which is expected to converge to a plateau for large enough source-sink separations. At the high pion masses used for the quenched ensembles, the vector state is stable, justifying the assumption of a plateau. For dynamical ensembles, we also compute an all-mode-average estimator for the latter quantity. The numerator C^{lc} is estimated using a sloppy full statistics estimator, which is then corrected by the difference between C^{lc} and the sloppy estimator computed for a few point sources. We estimate the denominator C^{ll} using the difference $C^{\mathrm{ll}} - C^{\mathrm{ll}}_{\mathrm{sloppy}}$, with the full statistics estimator $C^{\mathrm{ll}}_{\mathrm{sloppy}}$ restricted to the source positions from which the numerator C^{lc} is computed.

For quenched ensembles with periodic BC, each correlator was estimated using three Z_2 wall sources at lattice time 0. For quenched ensembles with open BC, the correlators were estimated using three such sources located at $T/2a$, except for the ensemble with $\beta = 3.0$ and a lattice volume of $32^3 \times 96$. For this ensemble, additional correlator measurements were performed at the beginning of the bulk to ensure enough time slices were available for reliable fits. For all ensembles, the correlators were folded by keeping the source-sink separation $t = 0$ fixed and averaging the time slices t and $T/a - t$ for $t = 1, \ldots, T/2a - 1$. For quenched periodic BC ensembles, we use a constant fit *Ansatz*

$$Z_V(t) = Z_V \tag{32}$$

with fit parameter Z_V. To determine the starting time slice of the fit range, we employ an extrapolation-based criterion to ensure that the fit function accurately models the data. We begin with small initial time slices and perform a fit to

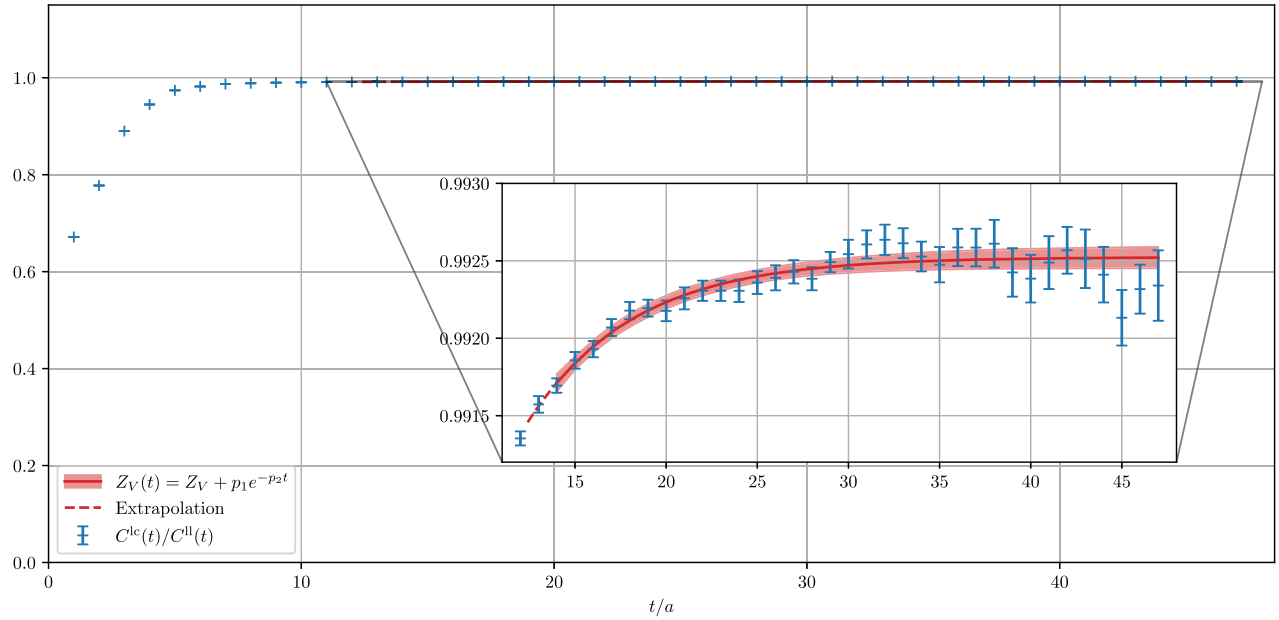

FIG. 4. Plateau fit of the ratio $C^{lc}(t)/C^{ll}(t)$ using the model $Z_V(t) = Z_V + p_1 e^{-p_2 t}$. This is shown for the quenched $\beta = 3.4$ ensemble with a lattice volume of $48^3 \times 192$.

the data over the selected range. Using this fit, the model value is extrapolated from the smallest time slice in the fit range to the next smaller time slice, which is not included in the fit. If the extrapolated value lies within approximately 1σ of the actual data point at that time slice, the fit range is considered valid. This process is repeated with incrementally larger initial time slices until the 1σ criterion is satisfied. The initial time slice of the largest fit range meeting this criterion is then used for the analysis.

The final time slice of the fit range is determined based on the availability of data. For periodic BC, it corresponds to the last available time slice of the folded correlator, while for open BC, it is limited by the bulk definition described in Sec. III A. If the fit prediction for the last time slice deviates by more than 1σ from the actual data point, the final time slice is adjusted to an earlier value until agreement within 1σ is achieved. Our choice of the final time slice is motivated by the possibility for lattice correlators to exhibit non-Gaussian statistical fluctuations at large time separations. To address this, we limit the maximum fit range, as described. Additionally, a second analysis group conducted the same analysis without imposing a specific criterion on the final time slice and obtained consistent results, further underscoring the robustness of our conclusions. For open BC quenched ensembles with a lattice volume of $24^3 \times 96$, we also consider a constant fit model. For quenched open BC ensembles with lattice volumes of $32^3 \times 96$ and $48^3 \times 192$, the fit range was limited by the bulk definition, prompting the use of a three-parameter fit model,

$$Z_V(t) = Z_V + p_1 e^{-p_2 t}, \tag{33}$$

with fit parameters Z_V, p_1, and p_2. This choice allowed for an extended fit range compared to the constant fit. An exemplary fit for $\beta = 3.4$ is shown in Fig. 4. To determine the normalization factors for the dynamical ensembles, we use a constant fit model, as the lattice volumes are sufficiently large to allow for this approach. The starting time slice of the fit range is chosen using the same extrapolation criterion as described above. However, due to increasing statistical noise at larger time slices, the final time slice is chosen such that the signal-to-noise ratio of the folded correlator remains larger than 10.

In Tables IV and V, we list the extracted normalization factors Z_V for the quenched and dynamical ensembles. The relative errors on Z_V are all smaller than 1 per mille, except for dynamical ensemble 4, where the relative error is slightly larger at 1.2 per mille. For the $\beta = 3.4$ ensemble shown in Fig. 4, the relative error is as small as 0.1 per mille. The vector correlators C^{ll} and C^{lc} are renormalized by multiplying them with a factor of Z_V^2 and Z_V, respectively. In the following discussions, we always consider the renormalized versions of the vector correlators.

G. Short-distance window a_μ^{SD}

To compute the short-distance window of the leading order HVP a_μ^{SD}, we need to evaluate the weighted sums

$$a_\mu^{\mathrm{SD},i} = \sum_{t=0}^{\infty} C^i(t) w_t^{\mathrm{SD}}, \tag{34}$$

where we introduced

TABLE IV. Normalization factors Z_V for quenched ensembles. The table presents the inverse coupling (β), the extracted normalization factor (Z_V), the lattice dimensions ($L^3 \times T/a^4$), and the BCs.

β	Z_V	$L^3 \times T/a^4$	BC
2.40	0.73849(55)	$24^3 \times 48$	Periodic
2.45	0.75470(35)	$24^3 \times 48$	Periodic
2.50	0.77212(57)	$24^3 \times 48$	Periodic
2.55	0.78712(48)	$24^3 \times 48$	Periodic
2.60	0.80160(29)	$24^3 \times 48$	Periodic
2.65	0.81645(17)	$24^3 \times 48$	Periodic
2.70	0.82967(19)	$24^3 \times 48$	Periodic
2.75	0.84413(26)	$24^3 \times 48$	Periodic
2.80	0.85646(16)	$24^3 \times 48$	Periodic
2.80	0.85689(17)	$24^3 \times 96$	Open
2.85	0.86918(17)	$24^3 \times 96$	Open
2.90	0.88155(17)	$24^3 \times 96$	Open
2.95	0.89367(17)	$24^3 \times 96$	Open
3.00	0.90544(17)	$24^3 \times 96$	Open
3.05	0.91713(16)	$24^3 \times 96$	Open
3.10	0.92848(11)	$24^3 \times 96$	Open
3.15	0.93953(15)	$24^3 \times 96$	Open
3.00	0.90565(14)	$32^3 \times 96$	Open
3.15	0.93958(12)	$32^3 \times 96$	Open
3.20	0.95075(56)	$32^3 \times 96$	Open
3.40	0.992523(72)	$48^3 \times 192$	Open

TABLE V. Normalization factors Z_V for dynamical ensembles. The table lists the ensemble ID, the extracted normalization factor (Z_V), the lattice dimensions ($L^3 \times T \times L_s/a^4$), and the BCs.

ID	Z_V	$L^3 \times T \times L_s/a^4$	BC
4	0.6999(12)	$24^3 \times 48 \times 24$	Periodic
9	0.73948(51)	$32^3 \times 64 \times 12$	Periodic
F	0.75735(88)	$48^3 \times 96 \times 12$	Periodic
E	0.79165(64)	$48^3 \times 192 \times 12$	Open

$$w_t^{\mathrm{SD}} = w_t[1 - \Theta(t, t_0 = 0.4\ \mathrm{fm}, \Delta = 0.15\ \mathrm{fm})] \tag{35}$$

and $C^i(t)$ denotes the renormalized vector correlators with $i \in \{\mathrm{ll}, \mathrm{lc}\}$. Additionally, we compute the same quantity with w_t^{SD} replaced by $\hat{w}_t^{\mathrm{SD}}$, which relies on the alternative weight definition from Eq. (8). The integrals in the weight computation are evaluated numerically. For the physical muon mass and fine structure constant, we considered the values provided in [23],

$$m_\mu = 0.1056583755(23)\ \mathrm{GeV}, \quad \text{and} \quad \alpha = 0.0072973525693(11). \tag{36}$$

Due to the finite temporal extent and bulk sizes of our lattices, a cutoff t_{max} is introduced in the weighted sum to study the resulting limitations,

$$a_\mu^{\mathrm{SD},i}(t_{\mathrm{max}}) = \sum_{t=0}^{t_{\mathrm{max}}} C^i(t) w_t^{\mathrm{SD}}. \tag{37}$$

For periodic BC ensembles, the maximum time slice included in the sum t_{max}^c is set to half the temporal lattice extent. In case of ensembles with open BC, the maximum time slice is determined by the bulk region. An exception to this rule applies to the open BC ensembles with a lattice volume of $32^3 \times 96$. For $\beta = 3.0$ and $\beta = 3.15$, the cumulative sums are directly compared with their small-volume counterparts (see Fig. 5). Since no boundary effects are observable when comparing the volumes, we set the maximum time slice for the large volumes to the same value as for the smaller volumes. In the case of $\beta = 3.2$, no small-volume counterpart exists, so we choose t_{max}^c, such that the physical size of the bulk is the same or smaller as for the large volume at $\beta = 3.15$. To account for the systematics introduced by the cutoff choice, we include an additional systematic error, calculated as the absolute difference between $a_\mu^{\mathrm{SD},i}(t_{\mathrm{max}}^c)$ and its value evaluated five time slices earlier.

IV. CONTINUUM LIMIT OF THE SHORT-DISTANCE WINDOW a_μ^{SD}

The main goal of this work is to compute the continuum limit of the short-distance contribution a_μ^{SD} to the leading-order HVP a_μ. To achieve this, we rely on the expectation that discretization effects in both dynamical and quenched simulations are similar, and that the short-distance window is mostly insensitive to variations in quark masses [16]. We propose performing a precise continuum limit using numerous quenched ensembles to get a quenched approximation of the short-distance contribution $a_\mu^{\mathrm{SD,q}}$. The parameters determined from this study will then be used as a prior to constrain the parameters of a separate dynamical continuum extrapolation. The advantage of this approach is that the quenched ensembles necessary to obtain a precise estimate of $a_\mu^{\mathrm{SD,q}}$ are computationally inexpensive compared to the corresponding dynamical estimates. The estimate of a_μ^{SD} can be determined by employing only a small number of expensive dynamical ensembles, matched with their quenched counterparts in terms of scale.

A. Quenched approximation

We start by discussing the continuum limit of the up and down quark-connected contributions to $a_\mu^{\mathrm{SD,q}}$. The continuum extrapolations of $a_\mu^{\mathrm{SD,q},i}$ are performed using separate fits for $i \in \{\mathrm{ll}, \mathrm{lc}\}$ and for the weights w_t and $\hat{w}_t$. Quantities determined with $\hat{w}_t$ are indicated with a hat. As described in Sec. III A, there are 21 independent data

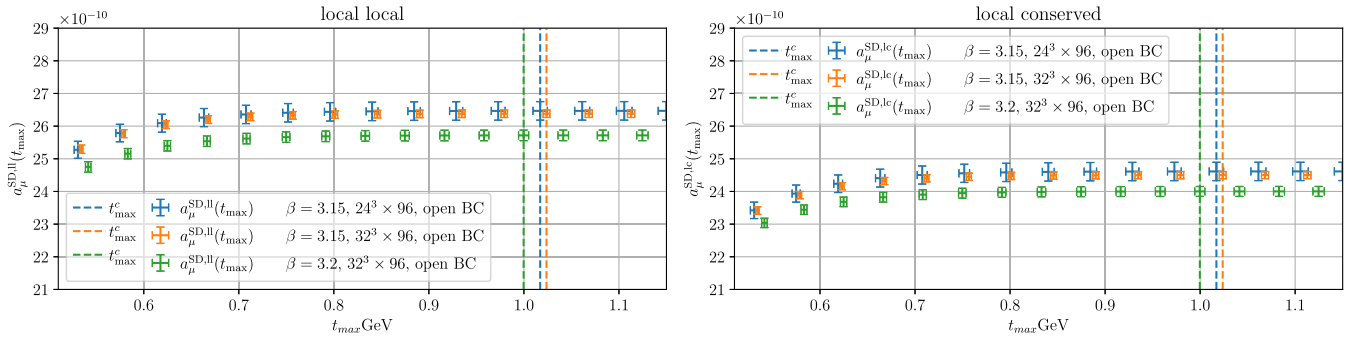

FIG. 5. Exemplary representation of the blinded weighted sums $a_\mu^{\mathrm{SD},i,\mathrm{blinded}}(t_{\mathrm{max}})$ computed with the weights w_t for $\beta = 3.15$ with lattice volume $24^3 \times 96$ and for $\beta = 3.15$ and $\beta = 3.2$ with lattice volume $32^3 \times 96$. The chosen cutoffs t_{max}^c are indicated with dashed lines. One the left, the blinded local-local measurements ($i = \mathrm{ll}$) are shown. On the right, the blinded local-conserved measurements ($i = \mathrm{lc}$) are displayed.

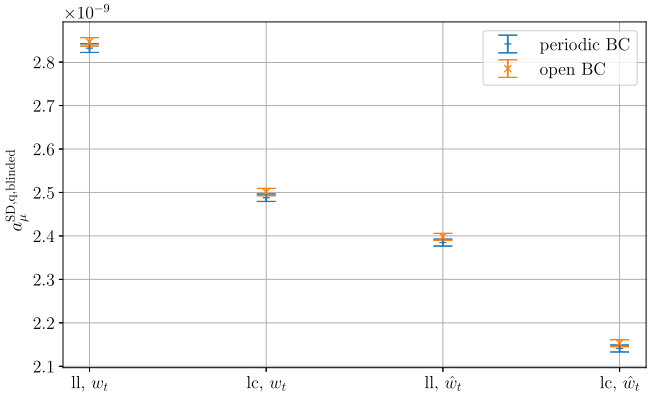

FIG. 6. Comparison of the $a_\mu^{\mathrm{SD,q,blinded}}$ estimates between the periodic BC and open BC ensembles at $\beta = 2.8$, computed using the weights w_t and $\hat{w}_t$ for both local-local (ll) and local-conserved (lc) correlators.

points available for both local-local and local-conserved measurements, respectively. For the inverse couplings $\beta = 2.8$, 3.0, 3.15, we choose to only include the measurements corresponding to the larger lattice volume, reducing the number to 18. At $\beta = 2.80$, two ensembles with identical parameters, differing only in T/a and the boundary conditions, are available. To validate the chosen bulk region for ensembles with open BC, we compared the computed values of $a_\mu^{\mathrm{SD,q,blinded}}$ for these two ensembles. As shown in Fig. 6, the results are compatible within uncertainties, indicating that the boundary conditions have no significant effect on our results. In Table VI, we show the results of a binning study for the finest ensembles ($\beta = 3.4$) to demonstrate that the autocorrelations are under control.

For the continuum extrapolation, we consider the following four fit *Ansätze*:

$$f_A^i(a^2) = A_0^i + A_1^i a^2 + A_2^i a^4, \tag{38a}$$

$$f_B^i(a^2) = B_0^i + B_1^i a^2 + B_2^i a^4 + B_3^i a^2 \log a^2, \tag{38b}$$

$$f_C^i(a^2) = C_0^i + C_1^i a^2 + C_2^i a^2 \log a^2, \tag{38c}$$

$$f_D^i(a^2) = D_0^i + D_1^i a^2 + D_2^i a^4 + D_3^i a^6, \tag{38d}$$

which are considered with fit parameters $A_\cdot^i$, $B_\cdot^i$, $C_\cdot^i$, $D_\cdot^i$, and $i \in \{\mathrm{ll}, \mathrm{lc}\}$. The models f_A^i and f_D^i represent pure polynomial fit *Ansätze*, while f_B^i and f_C^i incorporate a logarithmic term. An overview of all found χ^2-function minima χ_0^2 and the corresponding p-values is provided in Fig. 7, with the continuum results displayed in Fig. 8. Upon analyzing the blinded fit results, we observe a poor fit quality for f_A, as displayed in Fig. 9. This is indicated by the corresponding p-values: p_A^{ll}, p_A^{lc}, $\hat{p}_A^{\mathrm{ll}}$, and $\hat{p}_A^{\mathrm{lc}}$, all of which evaluate roughly to zero. Furthermore, we find a tension between the blinded local-local and local-conserved predictions, as well as between the values computed with w_t and those computed with $\hat{w}_t$. In contrast, the blinded fit results for the model f_B^i, shown in Fig. 10, exhibit a significantly better quality, as can be quantified by higher p-values: $p_B^{\mathrm{ll}} \approx 0.38$, $p_B^{\mathrm{lc}} \approx 0.21$, $\hat{p}_B^{\mathrm{ll}} \approx 0.33$, and $\hat{p}_B^{\mathrm{lc}} \approx 0.18$. Additionally, all continuum results for this model *Ansatz* agree within the error margins. The fit models f_C^i and f_D^i yield p-values that fall between those of models f_A^i and f_B^i, with f_D^i demonstrating better fit quality between the two. The corresponding fits are visualized in Fig. 11 for f_C^i and in Fig. 12 for f_D^i. However, the continuum results from f_D^i are not consistent, whereas those from f_C^i are. These observations suggest that including a logarithmic term is necessary to obtain consistent results for both local-local and local-conserved estimates. This confirms the expectation of a large logarithmic dependence, which without additional subtraction is even present at tree level [24–27].

To obtain an estimate for $a_\mu^{\mathrm{SD,q,blinded}}$, we employ a model averaging procedure. For this, we assign the following probability to each model M:

TABLE VI. Binning study for the short-distance contribution to the HVP $a_\mu^{\mathrm{SD,q,ll}}$ computed on the local-local vector correlator in the quenched approximation. The table columns show the rescaled standard deviations $\sigma_b(a_\mu^{\mathrm{SD,q,ll}})$ for the $\beta = 3.4$ ensemble with a lattice volume of $48^3 \times 96$ at bin sizes $b = 1, 2, 4, 8$. The standard deviations were scaled by a factor of 10^{11} and the value chosen for the analysis is indicated with a star. The maximum bin size for the study was chosen such that the binned samples contained at least 25 entries, ensuring a sufficiently small error in the estimated uncertainties.

	b = 1	b = 2	b = 4	b = 8
$\sigma_b(a_\mu^{\mathrm{SD,ll}}) \times 10^{11}$	1.12	1.17⋆	1.29	1.27

$$P(M) = \frac{\exp(-\mathrm{AIC}_M/2)}{\sum_{M'} \exp(-\mathrm{AIC}_{M'}/2)}, \tag{39}$$

where AIC_M denotes the value of the Akaike information criterion [28] for model M, with

$$\mathrm{AIC} = 2k + \chi_0^2, \tag{40}$$

and k represents the number of independent model parameters. This criterion rewards fit quality while penalizing a large number of parameters. Subsequently, we compute the model average for a fit parameter p as

$$\bar{p} = \sum_M P(M) p_M, \tag{41}$$

where p_M is the determined fit parameter for fit model M. The systematic variance for the model averaging is given by

$$\sum_M P(M)(p_M - \bar{p})^2. \tag{42}$$

Using this approach, our blinded result for the quenched approximation of the up and down quark-connected contribution to a_μ^{SD} is thus given by

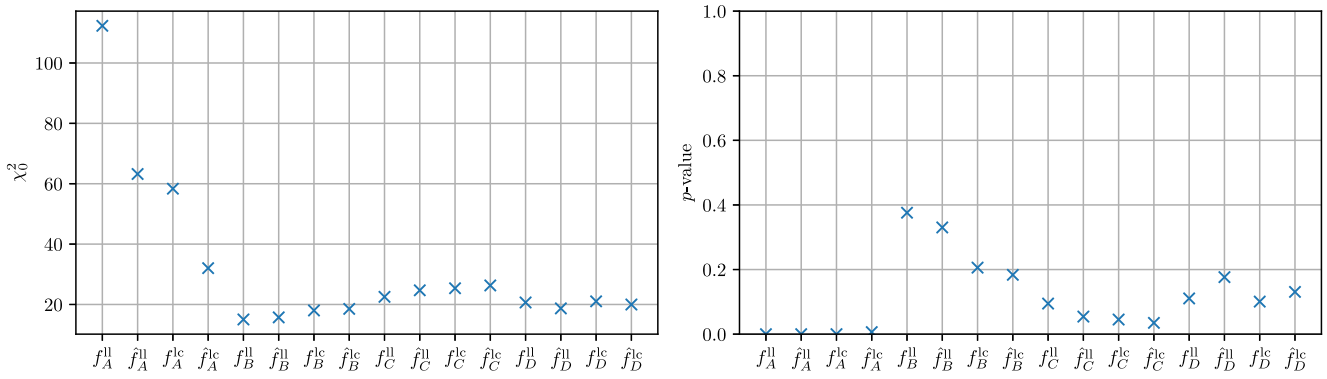

FIG. 7. Overview of the computed χ^2-function minima χ_0^2 (left) and p-values (right) for $a_\mu^{\mathrm{SD,q,blinded}}$. The fit models used for both weights w_t and $\hat{w}_t$ are f_A^i, f_B^i, f_C^i, and f_D^i, as defined in Eqs. (38a) to (38d). Fit results based on $\hat{w}_t$ are indicated by a hat.

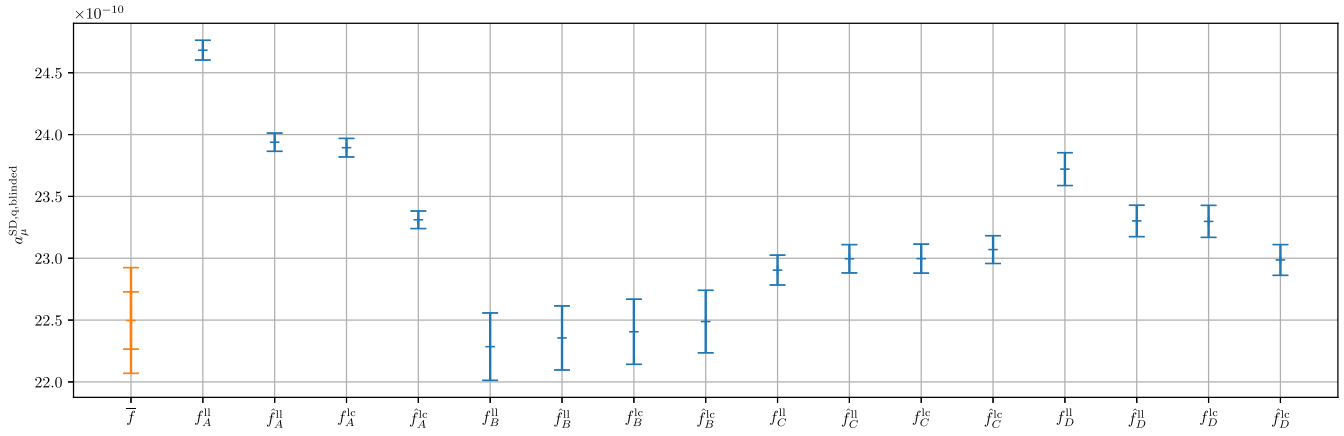

FIG. 8. Comparison of the model average for $a_\mu^{\mathrm{SD,q,blinded}}$, indicated by $\bar{f}$, with the estimates obtained from the quenched continuum extrapolations. The fit models used for both weights w_t and $\hat{w}_t$ are f_A^i, f_B^i, f_C^i, and f_D^i, as defined in Eqs. (38a) to (38d). Fit results based on $\hat{w}_t$ are indicated by a hat. The inner error bar for the model average $\bar{f}$ represents the statistical error, while the outer error bar shows the total error, which includes both statistical and systematic contributions.

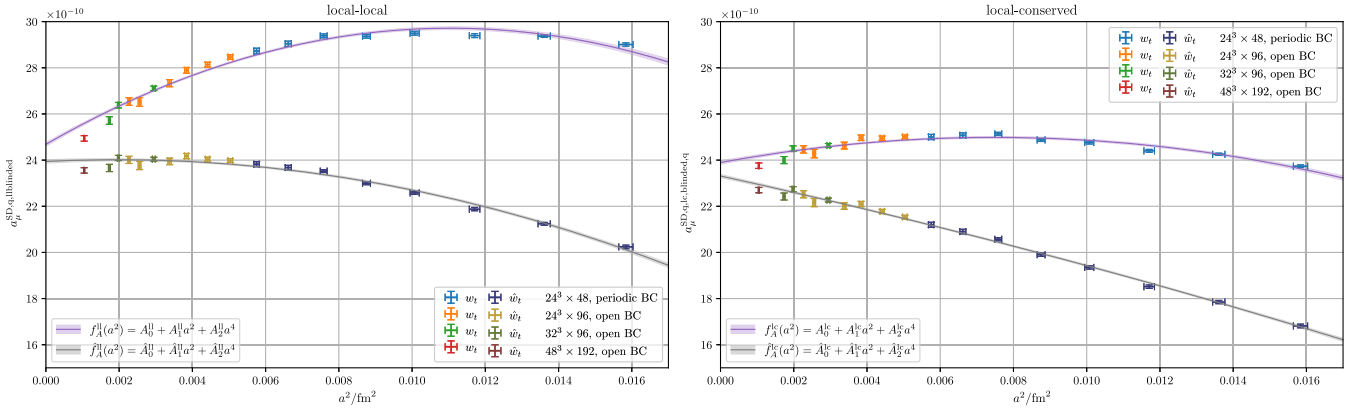

FIG. 9. Continuum extrapolations of $a_\mu^{\mathrm{SD,q}}$ computed with w_t and $\hat{w}_t$ using the polynomial fit model $f_A^i(a^2)$ from Eq. (38a). The model fit based on the $\hat{w}_t$ is denoted by $\hat{f}_A^i(a^2)$. On the left, we show the fits of the blinded local-local measurements, i.e., $i = \mathrm{ll}$. On the right, we display the fits of the blinded local-conserved measurements with $i = \mathrm{lc}$.

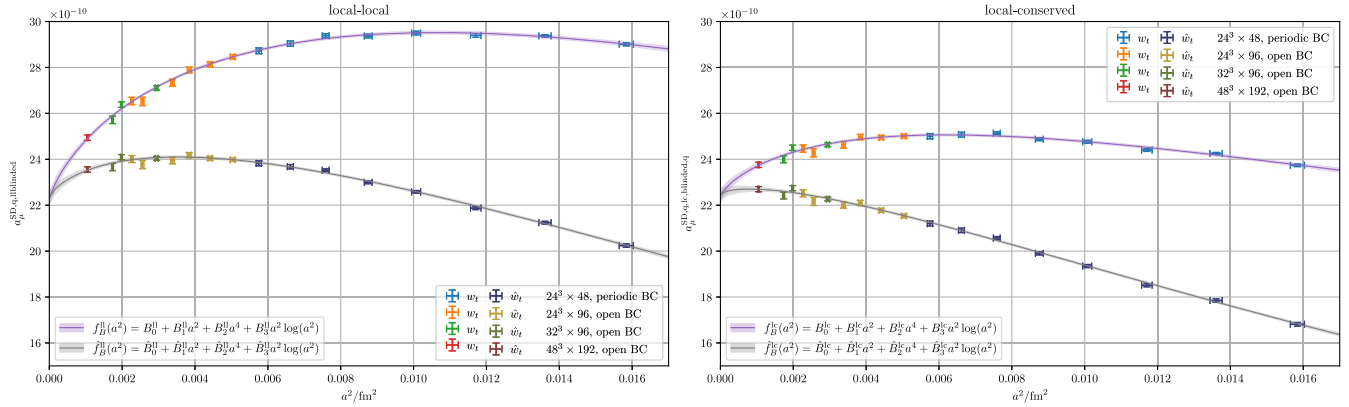

FIG. 10. Continuum extrapolations of $a_\mu^{\mathrm{SD,q}}$ computed with w_t and $\hat{w}_t$ using the polynomial fit model $f_B^i(a^2)$ from Eq. (38b), including a logarithmic term. The model fit based on the $\hat{w}_t$ is denoted by $\hat{f}_B^i(a^2)$. On the left, we show the fits of the blinded local-local measurements, i.e., $i = \mathrm{ll}$. On the right, we display the fits of the blinded local-conserved measurements with $i = \mathrm{lc}$. We stress that the agreement in the continuum limit between the local-local and local-conserved extrapolations is not enforced in the fit but is rather used as a check of consistency.

$$a_\mu^{\mathrm{SD,q,blinded}} = 22.50(23)(36) \times 10^{-10}. \tag{43}$$

As described at the end of Sec. III B, the value in the first parenthesis represents the statistical error, while the value in the second parenthesis denotes the total systematic error, which is dominated by the contribution from the systematic error arising in the model averaging procedure. In Fig. 8, the model average is compared to the estimates for $a_\mu^{\mathrm{SD,q,blinded}}$ from the individual fits. We intentionally quote the blinded result at this stage to emphasize that the analysis was performed without introducing unintended bias, particularly for the dynamical results where the value from previous studies is known. To further test the robustness of the fits and the model-averaging procedure, we performed an additional analysis by excluding the coarsest two lattice spacings ($\beta = 2.4$ and 2.45) from the dataset. Repeating the quenched analysis under this constraint yields the result

$$a_\mu^{\mathrm{SD,q,blinded,CUT}} = 22.77(16)(24) \times 10^{-10}. \tag{44}$$

This result is consistent with the original blinded result, demonstrating that the systematic uncertainties arising from the model averaging procedure remain robust with respect to cuts in the lattice spacing.

B. Dynamical estimate

As already mentioned in Sec. III C, the scale for our intermediate quenched world does not describe the real physical world. However, since we want to use the quenched results as input for the dynamical continuum limit, the scale of the quenched simulations has to be matched with the dynamical scale, which includes sea quark effects. We optimize the matching by aligning the contribution of $C(t)w_t$ at $t/a = 2$ to a_μ^{SD}, which effectively

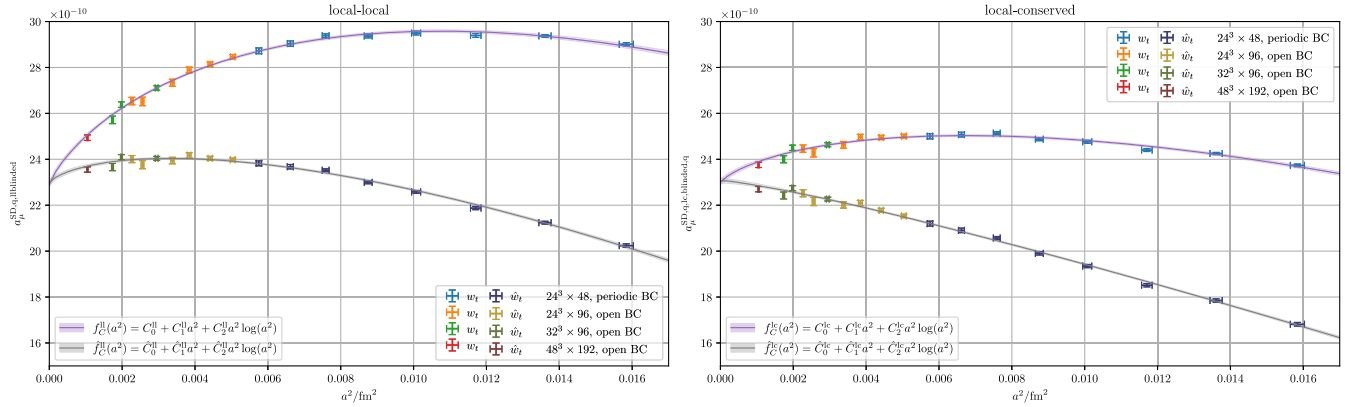

FIG. 11. Continuum extrapolations of $a_\mu^{\mathrm{SD,q}}$ computed with w_t and $\hat{w}_t$ using the polynomial fit model $f_C^i(a^2)$ from Eq. (38c), including a logarithmic term. The model fit based on the $\hat{w}_t$ is denoted by $\hat{f}_B^i(a^2)$. On the left, we show the fits of the blinded local-local measurements, i.e., $i = \mathrm{ll}$. On the right, we display the fits of the blinded local-conserved measurements with $i = \mathrm{lc}$. We stress that the agreement in the continuum limit between the local-local and local-conserved extrapolations is not enforced in the fit but is rather used as a check of consistency.

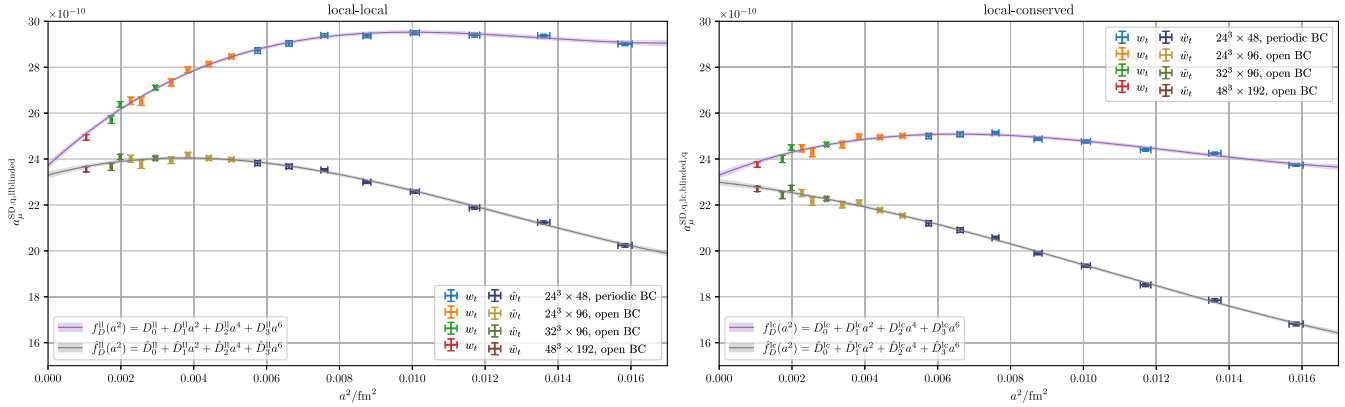

FIG. 12. Continuum extrapolations of $a_\mu^{\mathrm{SD,q}}$ computed with w_t and $\hat{w}_t$ using the polynomial fit model $f_D^i(a^2)$ from Eq. (38d). The model fit based on the $\hat{w}_t$ is denoted by $\hat{f}_A^i(a^2)$. On the left, we show the fits of the blinded local-local measurements, i.e., $i = \mathrm{ll}$. On the right, we display the fits of the blinded local-conserved measurements with $i = \mathrm{lc}$.

ensures the matching of the other short-distance time slices as well. This is achieved by rescaling the quenched scale $\sqrt{t_0^{\mathrm{q}}}$ to match the dynamical scale $\sqrt{t_0^{\mathrm{d}}}$. The muon mass is also appropriately rescaled. We refer to the rescaled quenched scale as $\sqrt{t_0^{\mathrm{r}}}$. A comparison of the a_μ^{SD} summand $C(t)w_t$ with $t/a = 2$ for the three scales is displayed in Fig. 13. This comparison indicates that the primary summands contributing to the short-distance contribution approach the continuum limit in a comparable fashion. Consequently, the model parameters describing the scale dependence for both the dynamical and quenched continuum extrapolations are expected to be similar.

Considering that only four dynamical ensembles (see Table II) are included in this study, we are restricted to fitting models with three parameters: f_A and f_C. Both models produce reasonable p-values ranging from 0.3 to 0.6, though the parameter variances are approximately 10% and the continuum results exhibit a spread. The continuum extrapolations for models f_A and f_C are presented in Fig. 14, while Fig. 15 provides an overview of the χ^2-function minima χ_0^2 and p-values. The continuum values and the AIC model average $\bar{f}$ are illustrated in Fig. 16. When comparing the second and the third model parameters for the fits using the quenched scale $\sqrt{t_0^{\mathrm{q}}}$, the rescaled quenched scale $\sqrt{t_0^{\mathrm{r}}}$, and the dynamical scale $\sqrt{t_0^{\mathrm{d}}}$, we found that these parameters agreed best when using the multiplicative fit *Ansätze*,

$$g_A^i(a^2) = A_0^i(1 + A_1^i a^2 + A_2^i a^4), \tag{45a}$$

$$g_C^i(a^2) = C_0^i(1 + C_1^i a^2 + C_2^i a^2 \log a^2), \tag{45b}$$

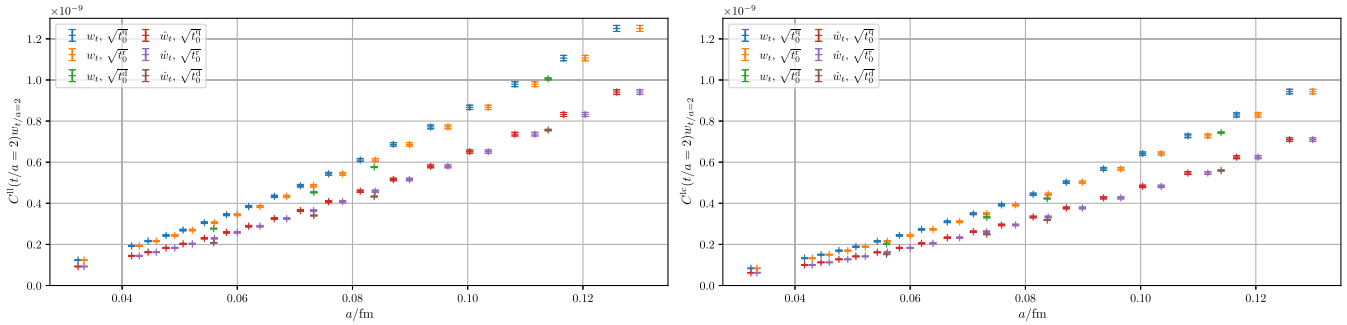

FIG. 13. Comparison of the blinded $a_\mu^{\rm SD}$ summand $C(t)w_t$ for $t/a = 2$ between the dynamical ensembles with scale $\sqrt{t_0^{\rm d}}$ and the quenched ensembles with the quenched scale $\sqrt{t_0^{\rm q}}$ and the rescaled quenched scale $\sqrt{t_0^{\rm r}}$. The summand is plotted versus the lattice spacing a in fm for both weight definitions w_t and $\hat{w}_t$. The left panel shows the local-local version, while the right panel displays the local-conserved version.

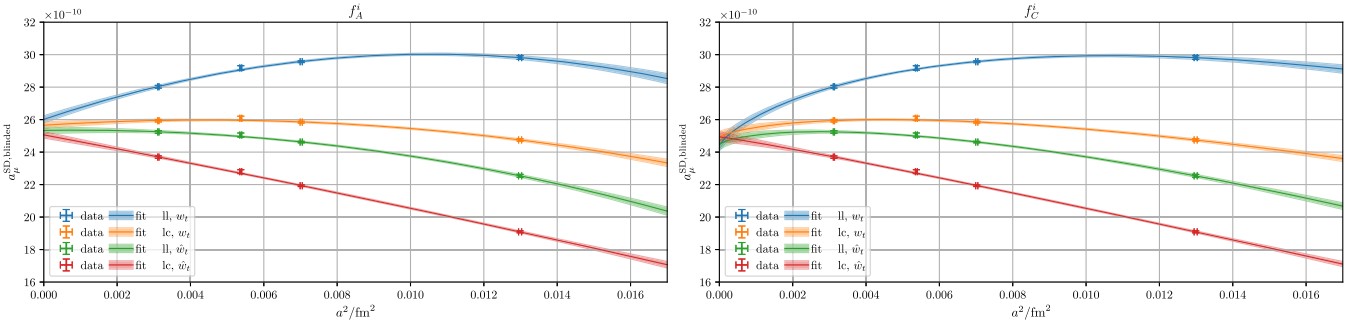

FIG. 14. Continuum extrapolations of the blinded ll and lc versions of $a_\mu^{\rm SD}$ using the weights w_t and $\hat{w}_t$. The left panel displays the fits for the model $f_A^i(a^2)$, as described in Eq. (38a), while the right panel shows the fits for the model $f_C^i(a^2)$ from Eq. (38c).

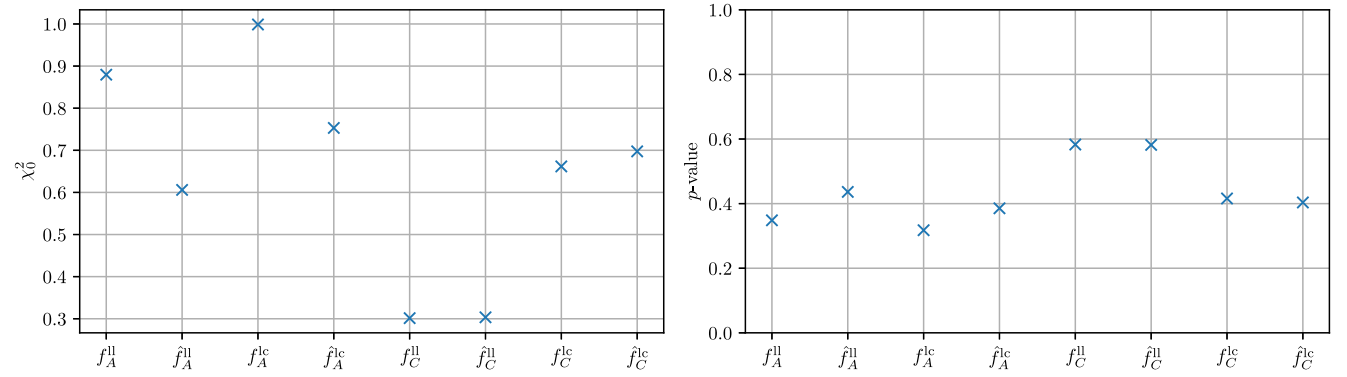

FIG. 15. Overview of the computed χ^2-function minima χ_0^2 (left) and p-values (right) for $a_\mu^{\rm SD,blinded}$. The fit models used for both weights w_t and $\hat{w}_t$ are f_A^i and f_C^i, as defined in Eqs. (38a) and (38c). Fit results based on $\hat{w}_t$ are indicated by a hat.

instead of Eqs. (38a) to (38c). We remark that using g^i instead of f^i amounts to a mere reparametrization of the same discretization and yields the same continuum result. Figure 17 shows that the quenched fit parameters for the rescaled scale $\sqrt{t_0^{\rm r}}$ are in good agreement with parameters for the dynamical scale $\sqrt{t_0^{\rm d}}$ in almost all cases. In cases where the match is not as precise, the parameters corresponding to the rescaled scale are still more closely aligned with the dynamical model parameters than with the original quenched scale parameters. This insight motivates us to constrain the parameters of the dynamical continuum extrapolation with the parameters of the quenched fits by adding the priors

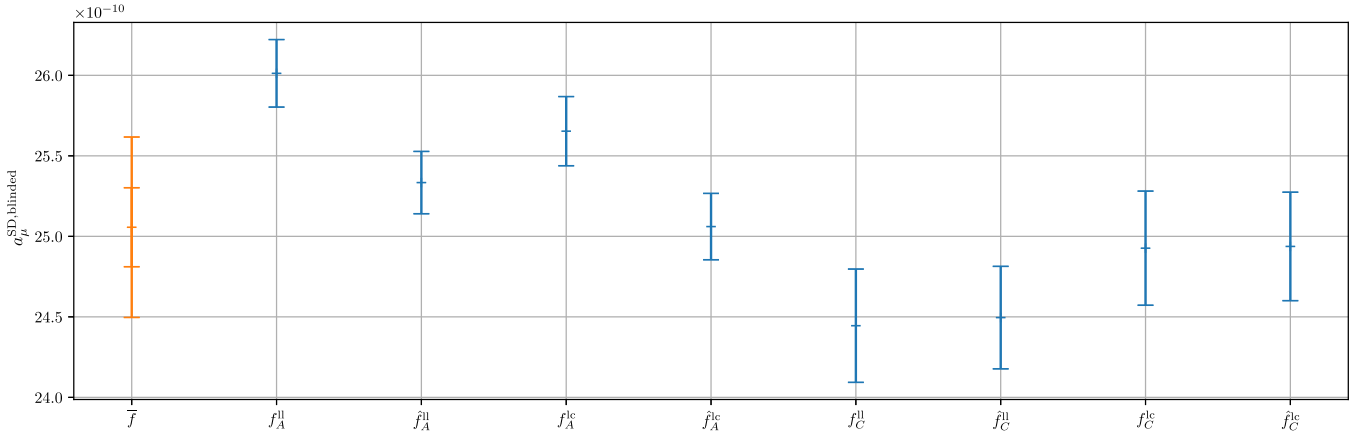

FIG. 16. Comparison of the model average for $a_\mu^{\mathrm{SD,blinded}}$, indicated by $\bar{f}$, with the estimates obtained from the continuum extrapolations. The fit models used for both weights w_t and $\hat{w}_t$ are f_A^i and f_C^i, as defined in Eqs. (38a) and (38c). Fit results based on $\hat{w}_t$ are indicated by a hat. The inner error bar for the model average $\bar{f}$ represents the statistical error, while the outer error bar shows the total error, which includes both statistical and systematic contributions.

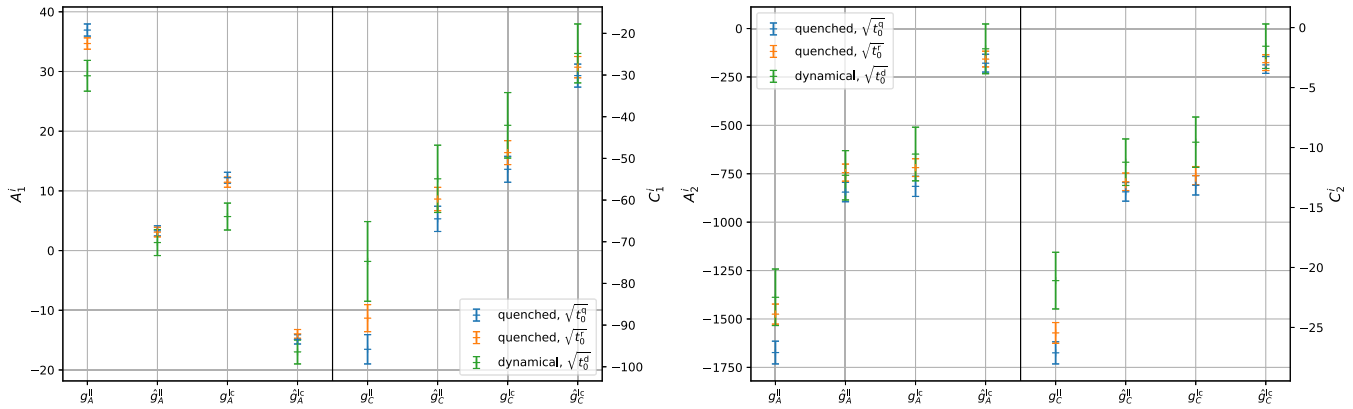

FIG. 17. Comparison of the fit parameters for the models $g_A^i(a^2)$ and $g_C^i(a^2)$ applied to $a_\mu^{\mathrm{SD,q}}$ using scales $\sqrt{t_0^{\mathrm{q}}}$ (blue) and $\sqrt{t_0^{\mathrm{r}}}$ (orange), and to a_μ^{SD} using scale $\sqrt{t_0^{\mathrm{d}}}$ (green). The left panel displays the first parameters A_1^i and C_1^i for both models, while the right panel shows the second parameters A_2^i and C_2^i. Fits based on data computed with $\hat{w}_t$ are indicated by a hat.

$$\sum_{k=1}^{2}\frac{(A_k^i - A_k^{i,\mathrm{q}})^2}{\mathrm{var}(A_k^{i,\mathrm{q}})} \quad \text{and} \quad \sum_{k=1}^{2}\frac{(C_k^i - C_k^{i,\mathrm{q}})^2}{\mathrm{var}(C_k^{i,\mathrm{q}})} \tag{46}$$

to the respective χ^2 functionals, where $A_k^{i,\mathrm{q}}$ and $C_k^{i,\mathrm{q}}$ denote the parameters of the corresponding quenched simulations with scale $\sqrt{t_0^{\mathrm{r}}}$ and fit models g_A^i and g_C^i.

We remark that the similarity between the quenched and dynamical model parameters is to be expected, as the difference of the discretization error between the quenched and dynamical short-distance contribution a_μ^{SD} to the anomalous magnetic moment is suppressed by two-loop perturbative QCD effects. However, this suppression is not the reason for constraining the dynamical fits, but rather serves as additional confirmation of the observed agreement. An overview of the χ^2-function minima χ_0^2 and p-values for the constrained dynamical fits is provided in Fig. 18. The errors on the constrained continuum results are reduced to approximately the same order of magnitude as in the quenched case, as expected, while still yielding p-values greater than 0.1 for all but two fits: g_A^{ll} and g_A^{lc}. This outcome may be explained for these two cases by the above observed discrepancy between the fit parameters for the dynamical scale and the rescaled quenched scale, as shown in Fig. 17. The constrained continuum extrapolations are shown in Fig. 19. The visible spread between the continuum results for the different discretizations and fit *Ansätze* is used in the AIC model averaging as an error estimate. Additionally, we note that we also performed constrained dynamical fits using the multiplicative model versions of f_B and f_D, defined as

$$g_B^i(a^2) = B_0^i(1 + B_1^i a^2 + B_2^i a^4 + B_3^i a^2 \log a^2), \tag{47a}$$

$$g_D^i(a^2) = D_0^i(1 + D_1^i a^2 + D_2^i a^4 + D_3^i a^6). \tag{47b}$$

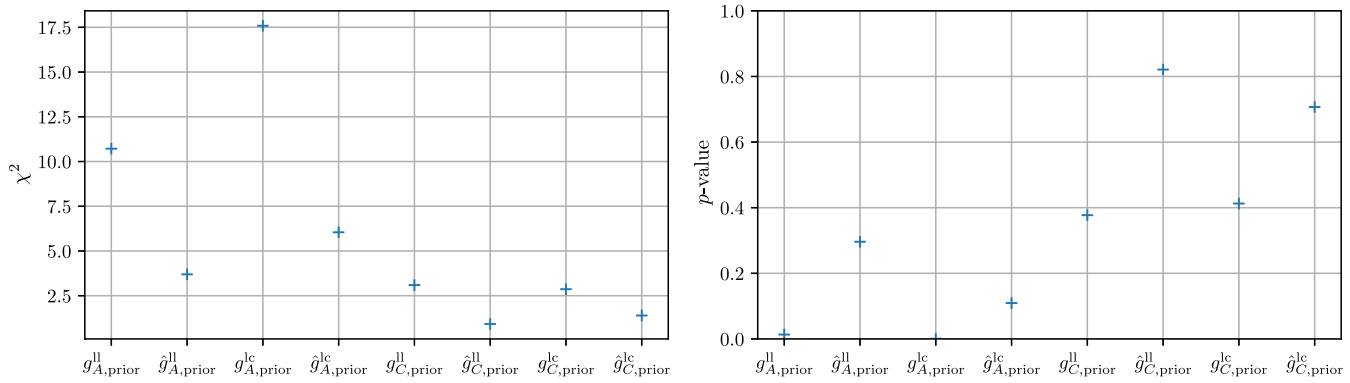

FIG. 18. Overview of the computed χ^2-function minima χ^2_0 (left) and p-values (right) for $a_\mu^{\mathrm{SD,blinded}}$. The fit models used for both weights w_t and $\hat{w}_t$ are g_A^i and g_C^i, as defined in Eqs. (45a) and (45b), with additional constraints on the second and third parameters using priors. We denote the corresponding fits as $g^i_{\cdot,\mathrm{prior}}$. Fit results based on $\hat{w}_t$ are indicated by a hat.

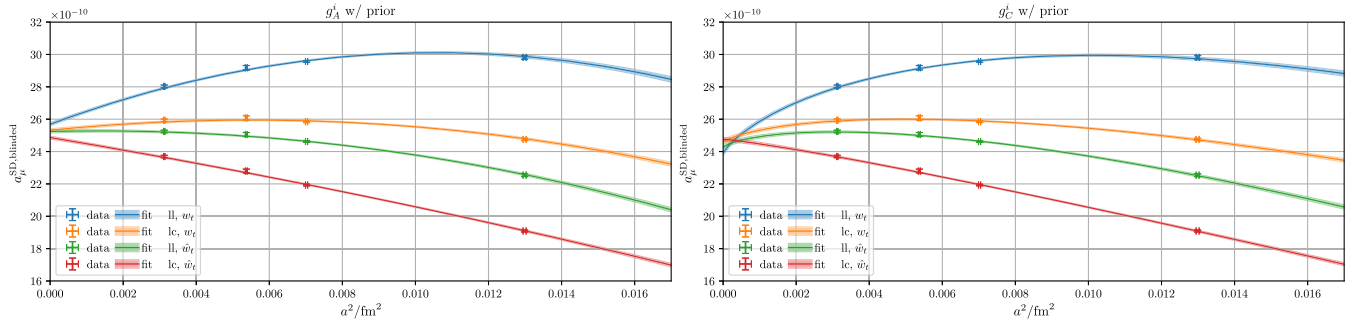

FIG. 19. Constrained continuum extrapolations of the blinded ll and lc versions of a_μ^{SD} using the weights w_t and $\hat{w}_t$. The left panel displays the fits for the model $g_A^i(a^2)$ [see Eq. (45a)] with priors, while the right panel shows the fits for the model $g_C^i(a^2)$ [see Eq. (45b)] with priors. In both fits, the second and third parameters are constrained to the values of their quenched counterpart fits.

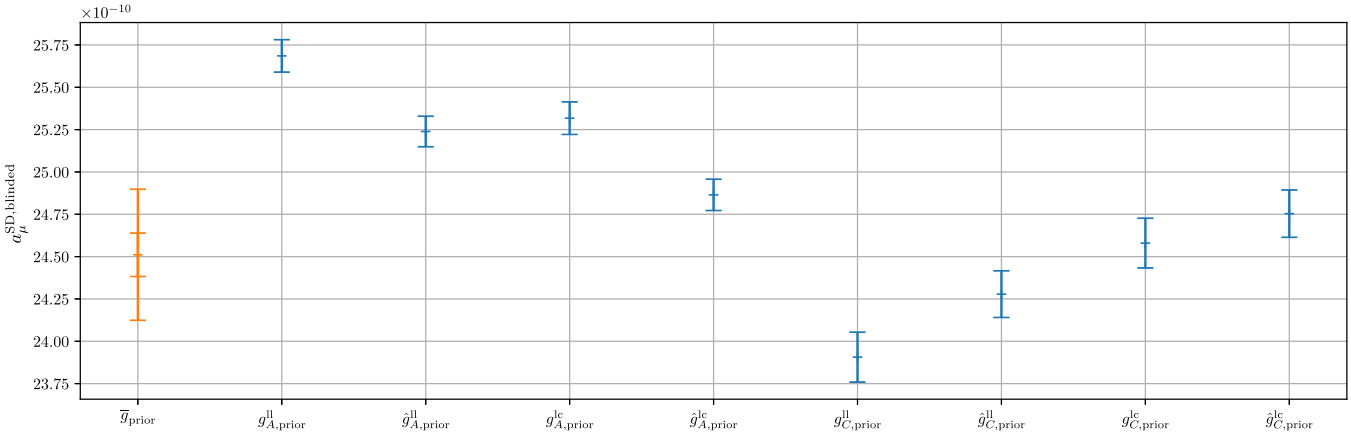

FIG. 20. Comparison of the model average for $a_\mu^{\mathrm{SD,blinded}}$, denoted as $\bar{g}_{\mathrm{prior}}$, with the estimates obtained from the constrained continuum extrapolations. The fit models used for both weights w_t and $\hat{w}_t$ are g_A^i and g_C^i, as defined in Eqs. (45a) and (45b), with additional constraints on the second and third parameters using priors. We denote the corresponding fits as $g^i_{\cdot,\mathrm{prior}}$. Fit results based on $\hat{w}_t$ are indicated by a hat. The inner error bar for the model average $\bar{g}_{\mathrm{prior}}$ represents the statistical error, while the outer error bar shows the total error, which includes both statistical and systematic contributions.

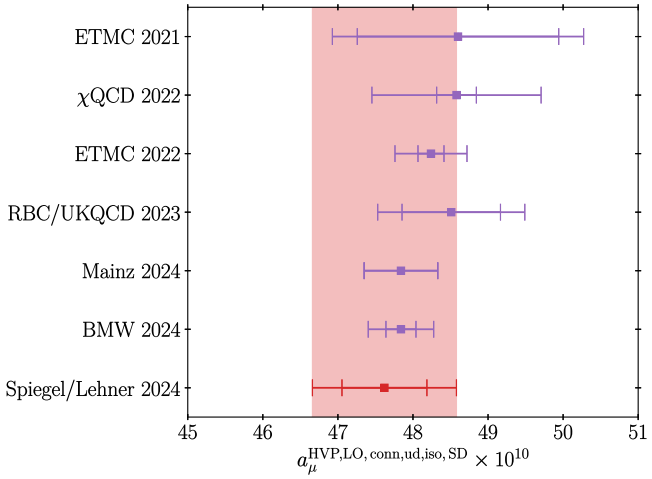

FIG. 21. Comparison of our result with existing literature: ETMC 2021 [32], χQCD 2022 [33], ETMC 2022 [29], RBC/UKQCD 2023 [34], Mainz 2024 [30], and BMW 2024 [31]. The inner error bars represent the statistical uncertainty, while the outer error bars show the statistical and systematic uncertainties added in quadrature.

These constrained fits are feasible in spite of the low number of data points, as the inclusion of priors in the Bayesian approach effectively adds data points. However, these models yield vanishing p-values in our analysis and, therefore, do not contribute significantly to the model average. Consequently, our model average for the constrained dynamical fits comprises eight results, all of which are displayed in Fig. 20.

After all checks were completed, we unblinded the results on July 22. Finally, we need a correction from the ≈280 MeV pion mass of the dynamical ensembles used in this work to the physical pion mass, which was calculated for the RBC/UKQCD23 SD window in Ref. [16],

$$\Delta a_\mu^{\mathrm{SD,mass}} = 0.41(4) \times 10^{-10}. \tag{48}$$

Our final unblinded result for the light-quark-connected short-distance window in the isospin symmetric limit is

$$a_\mu^{\mathrm{ud,iso,SD}} = 47.62(0.32)_{\mathrm{stat}}(0.60)_{\mathrm{syst}} \times 10^{-10}. \tag{49}$$

V. CONCLUSIONS AND OUTLOOK

In this study, we computed the short-distance Euclidean window of the hadronic vacuum polarization. To prevent potential bias toward previously published results, we employed a blinding procedure involving two independent analysis groups. The focus of this work was on the dominant quark-connected, light-quark, isospin-symmetric contribution, scrutinizing its continuum limit from first-principles lattice QCD without perturbative input. A precise quenched study revealed the necessity of a logarithmic dependency to obtain consistent continuum results across different discretizations, in agreement with the expectation [24–27]. We subsequently demonstrated that these quenched parameter results could be used to constrain the parameters of the corresponding dynamical continuum extrapolations. Our result for the short-distance window $a_\mu^{\mathrm{ud,iso,SD}}$, derived from the model average of these constrained continuum limits, is consistent with recently published results that rely on perturbative input, as shown in Fig. 21. However, our error estimate is significantly larger compared to the results of [29–31].

There are many directions one may explore in future work. For instance, one may include an additional dynamical ensemble with a finer lattice spacing compared to the currently available ones. This would allow us to achieve higher precision and further scrutinize the continuum limit. Additionally, one may systematically compare our results against perturbative calculations. This would involve tuning the lower cutoff of the short-distance window to ensure a robust and detailed comparison.

ACKNOWLEDGMENTS

We thank our colleagues from RBC/UKQCD collaborations for valuable discussions. We acknowledge computing resources provided at the University of Regensburg on the QPace3 and QPace4 clusters. The authors gratefully acknowledge the Gauss Centre for Supercomputing e.V. [35] for funding this project by providing computing time on the GCS Supercomputer JUWELS at Jülich Supercomputing Centre (JSC). We gratefully acknowledge disk and tape storage provided by the University of Regensburg with support from the DFG.

DATA AVAILABILITY

Some of the data that support the findings of this article are openly available [36,37]. Lattice gauge configurations are not publicly available upon publication because it is not technically feasible and/or the cost of preparing, depositing, and hosting the data would be prohibitive within the terms of this research project. Correlators are not publicly available. The data are available from the authors upon reasonable request.

[1] B. Abi *et al.* (Muon g-2 Collaboration), Measurement of the positive muon anomalous magnetic moment to 0.46 ppm, Phys. Rev. Lett. **126**, 141801 (2021).

[2] D. P. o. Aguillard (The Muon g-2 Collaboration), Measurement of the positive muon anomalous magnetic moment to 0.20 ppm, Phys. Rev. Lett. **131**, 161802 (2023).

[3] G. W. Bennett *et al.* (Muon g-2 Collaboration), Final report of the E821 muon anomalous magnetic moment measurement at BNL, Phys. Rev. D **73**, 072003 (2006).

[4] T. Aoyama *et al.*, The anomalous magnetic moment of the muon in the standard model, Phys. Rep. **887**, 1 (2020).

[5] M. Abe *et al.*, A new approach for measuring the muon anomalous magnetic moment and electric dipole moment, Prog. Theor. Exp. Phys. **2019**, 053C02 (2019).

[6] T. Blum, P. Boyle, V. Gülpers, T. Izubuchi, L. Jin, C. Jung, A. Jüttner, C. Lehner, A. Portelli, and J. Tsang, Calculation of the hadronic vacuum polarization contribution to the muon anomalous magnetic moment, Phys. Rev. Lett. **121**, 022003 (2018).

[7] D. Bernecker and H. B. Meyer, Vector correlators in lattice QCD: Methods and applications, Eur. Phys. J. A **47**, 148 (2011).

[8] S. Duane, A. Kennedy, B. J. Pendleton, and D. Roweth, Hybrid Monte Carlo, Phys. Lett. B **195**, 216 (1987).

[9] I. Omelyan, I. Mryglod, and R. Folk, Symplectic analytically integrable decomposition algorithms: Classification, derivation, and application to molecular dynamics, quantum and celestial mechanics simulations, Comput. Phys. Commun. **151**, 272 (2003).

[10] R. Sommer, Scale setting in lattice QCD, Proc. Sci. LATTICE2013 (**2014**) 015 [arXiv:1401.3270].

[11] M. Bruno and R. Sommer, On the n_f-dependence of gluonic observables, Proc. Sci. LATTICE2013 (**2014**) 321 [arXiv:1311.5585].

[12] M. Lüscher, Properties and uses of the Wilson flow in lattice QCD, J. High Energy Phys. 08 (2010) 071.

[13] R. C. Brower, H. Neff, and K. Orginos, The Möbius domain wall fermion algorithm, Comput. Phys. Commun. **220**, 1 (2017).

[14] Y. Shamir, Chiral fermions from lattice boundaries, Nucl. Phys. **B406**, 90 (1993).

[15] V. Furman and Y. Shamir, Axial symmetries in lattice QCD with kaplan fermions, Nucl. Phys. **B439**, 54 (1995).

[16] T. Blum, P. A. Boyle, M. Bruno, D. Giusti, V. Gülpers, R. C. Hill, T. Izubuchi, Y. C. Jang, L. Jin, C. Jung, A. Jüttner, C. Kelly, C. Lehner, N. Matsumoto, R. D. Mawhinney, A. S. Meyer, and J. T. Tsang, An update of euclidean windows of the hadronic vacuum polarization, arXiv:2301.08696.

[17] S. Borsányi, S. Dürr, Z. Fodor, C. Hoelbling, S. D. Katz, S. Krieg, T. Kurth, L. Lellouch, T. Lippert, C. McNeile, and K. K. Szabó, High-precision scale setting in lattice QCD, J. High Energy Phys. 09 (2012) 010.

[18] T. Blum, P. Boyle, N. Christ, J. Frison, N. Garron, R. Hudspith, T. Izubuchi, T. Janowski, C. Jung, A. Jüttner, C. Kelly, R. Kenway, C. Lehner, M. Marinkovic, R. Mawhinney, G. McGlynn, D. Murphy, S. Ohta, A. Portelli, C. Sachrajda, and A. Soni, Domain wall QCD with physical quark masses, Phys. Rev. D **93**, 074505 (2016).

[19] T. DeGrand and S. Schaefer, Improving meson two-point functions by low-mode averaging, Nucl. Phys. B, Proc. Suppl. **140**, 296 (2005).

[20] G. S. Bali, S. Collins, and A. Schäfer, Effective noise reduction techniques for disconnected loops in lattice QCD, Comput. Phys. Commun. **181**, 1570 (2010).

[21] T. Blum, T. Izubuchi, and E. Shintani, New class of variance-reduction techniques using lattice symmetries, Phys. Rev. D **88**, 094503 (2013).

[22] E. Shintani, R. Arthur, T. Blum, T. Izubuchi, C. Jung, and C. Lehner, Covariant approximation averaging, Phys. Rev. D **91**, 114511 (2015).

[23] R. L. Workman *et al.* (Particle Data Group), Review of particle physics, Prog. Theor. Exp. Phys. **2022**, 083C01 (2022).

[24] T. Harris, M. Cè, H. B. Meyer, A. Toniato, and C. Török, Vacuum correlators at short distances from lattice QCD, Proc. Sci. LATTICE2021 (**2021**) 572.

[25] M. Cè, T. Harris, H. B. Meyer, A. Toniato, and C. Török, Vacuum correlators at short distances from lattice QCD, J. High Energy Phys. 12 (2021) 215.

[26] R. Sommer, L. Chimirri, and N. Husung, Log-enhanced discretization errors in integrated correlation functions, Proc. Sci. LATTICE2022 (**2023**) 358 [arXiv:2211.15750].

[27] N. Husung, Logarithmic corrections to O(a) and O(a^2) effects in lattice QCD with Wilson or Ginsparg–Wilson quarks, Eur. Phys. J. C **83**, 142 (2023); **83**, 144(E) (2023).

[28] H. Akaike, A new look at the statistical model identification, IEEE Trans. Autom. Control **19**, 716 (1974).

[29] C. Alexandrou *et al.* (Extended Twisted Mass Collaboration), Lattice calculation of the short and intermediate time-distance hadronic vacuum polarization contributions to the muon magnetic moment using twisted-mass fermions, Phys. Rev. D **107**, 074506 (2023).

[30] S. Kuberski, M. Cè, G. von Hippel, H. B. Meyer, K. Ottnad, A. Risch, and H. Wittig, Hadronic vacuum polarization in the muon g −2: The short-distance contribution from lattice QCD, J. High Energy Phys. 03 (2024) 172.

[31] A. Boccaletti *et al.*, High precision calculation of the hadronic vacuum polarisation contribution to the muon anomaly, arXiv:2407.10913.

[32] D. Giusti and S. Simula, Window contributions to the muon hadronic vacuum polarization with twisted-mass fermions, Proc. Sci. LATTICE2021 (**2022**) 189.

[33] G. Wang, T. Draper, K.-F. Liu, and Y.-B. Yang (chiQCD Collaboration), Muon g-2 with overlap valence fermions, Phys. Rev. D **107**, 034513 (2023).

[34] T. Blum *et al.* (RBC and UKQCD Collaborations), Update of Euclidean windows of the hadronic vacuum polarization, Phys. Rev. D **108**, 054507 (2023).

[35] https://www.gauss-centre.eu/

[36] C. Lehner, Grid PYTHON toolkit, https://github.com/lehner/gpt.

[37] S. Spiegel, PYTHON toolkit targeted at lattice QCD data analysis, https://github.com/spieseba/statpy.